Satellite-based Time-Series of Sea Surface Salinity designed for Ocean and Climate Studies

J. Boutin[1], N. Reul[2], J. Koehler[3], A. Martin[4], R. Catany[5], S. Guimbard[6], F. Rouffi[7], J.L. Vergely[7], M. Arias[5], M. Chakroun[7], G. Corato[8], V. Estella-Perez[1,*], A. Hasson[1,†], S. Josey[4], D. Khvorostyanov[1], N. Kolodziejczyk[2], J. Mignot[1], L. Olivier[1], G. Reverdin[1], D. Stammer[3], A. Supply[1,2], C. Thouvenin-Masson[1], A. Turiel[9], P. Cipollini[10, ‡], C. Donlon[10, ‡], R. Sabia[11], S. Mecklenburg[10]

[1]Sorbonne University, LOCEAN/IPSL Laboratory, CNRS–IRD–MNHN, Paris, France.

[2]University of Brest, LOPS Laboratory, IUEM, UBO–CNRS–IRD–Ifremer, Plouzané, France.

[3]Institut für Meereskunde, Centrum für Erdsystemwissenschaften und Nachhaltigkeit, Universität Hamburg, Germany.

[4]National Oceanography Centre, Southampton, UK.

[5]ARGANS Ltd, UK.

[6]Ocean Scope, France.

[7]ACRI-st, France.

[8]Adwaiseo, Luxemburg.

[9]Barcelona Expert Center (BEC) and Institute of Marine Sciences (ICM), CSIC, Spain.

[10]European Space Agency, ECSAT, Harwell, United Kingdom.

[11]Telespazio-UK for ESA, ESRIN, Frascati, Italy.

Corresponding author: Jacqueline Boutin (`jb@locean.ipsl.fr`)

*Now at UL Services Spain SL

†Now at Mercator Ocean International, France

‡Now at European Space Agency, ESTEC, Noordwijk, the Netherlands.

Key Points:

- Well-established need for Sea Surface Salinity global fields at resolution better than 1 month, 1°
- 2010-2019 sea surface salinity fields built from three satellite missions data sets
- Monitoring of large mesoscale to basin wide sea surface salinity variability with unprecedented accuracy and spatio-temporal coverage

Abstract

Sea Surface Salinity (SSS) is an Essential Ocean and Climate Variable, which is increasingly used as part of climate studies. SSS measurements are available from three satellite missions, SMOS, Aquarius and SMAP, each with very different instrument features leading to specific measurement characteristics. The Climate Change Initiative Salinity project (CCI+SSS) aims to produce SSS Climate Data Record (CDR) to include satellite measurements, based on well-established user needs. To generate a homogeneous CDR, instrumental differences are carefully controlled by analysing SSS discrepancies, then adjusted based on in-depth analysis of the measurements themselves together with independent reference data. However, no spatial smoothing or temporal relaxation to reference data is applied in order to maintain the variability contained in the original data set. SSS CCI fields are well suited for monitoring weekly to interannual variability from the ocean basin scale to the large mesoscale. Thus, they depict that over the 2010-2019 decade, seasonal have varied greatly from year to year, sometimes by more than +/-0.4 over large regions. When monthly SSS CCI are compared with in situ Argo salinities, the robust standard deviation of their difference, at global scale, is 0.15, while r^2 is 0.97. This high level of performance highlights the benefit of the SSS CCI merging approach compared to individual satellite SSS fields alone. The correlation with independent ship SSS (r^2>0.9) further highlights the excellent performance of the data set. SSS CCI data are freely available and will be updated and extended in the future as more satellite data become available.

Plain Language Summary

Salinity characterizes the mass of salts in sea water. Salinity, together with temperature and pressure, determines the sea water density. In turn, density drives crucial motion in the ocean. At the ocean surface, a salinity decrease can be the result of freshwater inputs such as rain, river runoffs and ice melt. Reversely, surface salinity can trace evaporation. The salinity imprint of these processes is then carried by ocean currents over long distances and long periods of time. The large variations thus generated can impact ocean circulation through density and, at the sea surface, ocean-atmosphere exchanges of heat and gas. Hence, Sea Surface Salinity (SSS) is a key variable for ocean and climate studies both as a tracer and an actor of observed changes.

Since 2010, three satellite missions have monitored SSS with an unprecedented spatial resolution and temporal revisit. For the first time, data from these satellites are combined, after adjusting specific instrumental features. The resulting dataset enables the SSS to be monitored and studied with unprecedented accuracy over 2010-2019 and over the global ocean at a 50km, weekly or monthly resolution. It reveals particularly well large SSS variability related to phenomena affecting climate in various parts of the world.

1 Introduction

Salinity is a key ocean and climate variable that plays a fundamental role in

the thermohaline global ocean circulation, the hydrological cycle, and climate variability (Durack et al., 2012; Siedler et al., 2001).

Along with temperature, the salinity contributes to sea water density. This parameter influences the ocean stratification, water masses formation and ultimately the general circulation of the ocean. At high latitudes, in cold polar surface waters (typically T = 2°C), a change of 0.11 in Sea Surface Salinity [1,2] (SSS), is equivalent, in terms of density, to a change of 1°C in Sea Surface Temperature (SST). In warm regions (T=28°C), a larger salinity change of 0.44 is equivalent to a 1°C change in SST, as per its density contribution. This is the reason why salinity variations play a key role at high latitudes in controlling the global thermohaline circulation, transporting, in particular, waters from the ocean surface to the deep ocean. SSS bears the signature of freshwater fluxes originating from evaporation minus precipitation (E-P), river discharges and ice melting or freezing. Freshwater fluxes can modify the vertical stratification in density and strongly influence the air-sea exchange through the development of the so-called salt-stratified (halocline) barrier layers (Lukas and Lindstrom, 1991). Indirectly, salinity contributes to El-Nino Southern Oscillation (ENSO) (Vialard and Delecluse, 1998), Indian Monsoon (Shenoi et al., 2002) and primary productivity (Picaut et al., 2001). At high latitude the sharp halocline shields the heat stored in the deep ocean from reaching the surface layer and melting the sea ice (Carmack et al., 2016; Lique, 2015).

The ocean is a major component of the Earth's water cycle: 86% of evaporation and 78% of precipitation take place over the ocean. The near surface salinity is changing on global and basin scales, with an increase in the more evaporative regions and a decrease in the precipitation dominated regions, and this so-called 'dry gets dryer and wet gets wetter' tendency is also observed in climate projections (Bindoff et al., 2019; Yu et al., 2020). Both positive and negative trends in ocean salinity and freshwater content have been observed throughout much of the ocean including sea surface and ocean interior, providing indirect evidence that the E – P pattern over the oceans is amplifying. In addition, evaporated water above the ocean is transported above the continents by the atmospheric circulation. Li et al. (2016) recently found correlations between satellite SSS anomalies in the North Atlantic and anomalies of rain in Sahel lagged by several months suggesting that large scale SSS anomalies could bring skill as precursor indicators of rain over the continents.

In addition, being the total mass of dissolved salts in 1 kg of seawater, salinity affects the entire oceanic carbonate system and its components: total alkalinity,

[1]Sea Surface Salinity in this article refers to the salinity determined from a satellite microwave radiometer sensing the thermal emission at 1.4GHz due to its changing dielectric properties. Thus the measured quantity is representative of the upper few cm of the sea surface depending on the depth of surface foam present on the sea surface.

[2]Sea Surface Salinity is expressed with no physical units. It is defined according to the Practical Salinity Scale (UNESCO, 1985) as conductivity ratio: a seawater sample of Practical Salinity 35 has a conductivity ratio of 1.0 at 15°C and 1 atmosphere pressure, using a potassium chloride (KCl) standard solution containing a mass of 32.4356 grams of KCl per Kg of solution.

dissolved inorganic carbon, pH, and fugacity of CO_2 (Millero, 2007).

SSS has therefore been identified as an Essential Climate Variable (ECV) (https://public.wmo.int/en/programmes/global-climate-observing-system/essential-climate-variables).

SSS measurement by satellite remote sensing was motivated by the essential need of better monitoring, understanding and constraining the marine components of the water cycle and ocean circulation, air-sea interactions, as well as upper ocean biogeochemical state. At the end of the 1990s, the Global Ocean Data Assimilation Experiment (GODAE) group estimated that it was necessary to measure SSS with an accuracy of 0.1 at monthly, 100 km (or every 10 days at 200 km) scales. Since the beginning of the 21st century, the Argo network of in-situ profiling floats has continuously evolved (Roemmich et al., 2019) and provided unvaluable measurements of 3D oceanic salinity. The Argo array reached global coverage in 2006 with one measurement of both temperature and salinity every ~10 days and every ~300 km with a vertical sampling range of between about 5 - 2000m depth. Nevertheless, there is increasing consensus that the GODAE specifications that are well covered by the Argo network do not serve all the needs for ocean and climate studies. The analysis of ship measurements (Delcroix et al., 2005), and later of satellite measurements have revealed a natural variability of SSS much larger than 0.1 in regions characterized by large mesoscale variations (Fournier et al., 2016; Hasson et al., 2019; Reul et al., 2014), in river plumes and in areas characterized by strong precipitation events (e.g. Figure 6 in Boutin et al. 2016). In these regions, SSS fields derived from satellite data depict SSS variability much better than the salinity products derived from the in situ Argo network alone (Fournier and Lee, 2021).

Satellite SSS data are available with regular repeat global coverage since 2010, owing to microwave radiometers operating at a frequency of 1.4 GHz (wavelength 21 cm; L-Band). The brightness temperature (Tb) measured by ocean observing microwave radiometers is related to the emissivity of the ocean surface layer. At L-Band, Tb depends primarily on the dielectric properties of the surface seawater (i.e., seawater conductivity and, thus, salinity and temperature) and on its geometric characteristics, determined by sea surface roughness (Reul et al., 2020). At this frequency, the atmosphere is almost transparent (except for strong precipitation). Molecular oxygen has the most significant effect on the measured Tb with small contributions from water vapor, cloud liquid water, and rain. Tb has a relatively low sensitivity to SSS (~0.8 K (at SST=30°C) to ~0.2 K (at SST=0°C) per salinity unit) depending on the SST (Yueh et al., 2001). With a significantly weaker sensitivity of Tb to SSS, radiometer measurements of SSS in cold waters at high latitudes are particularly challenging placing strong requirement on noise equivalent difference temperature (NEdT).

SSS measured from satellites is not directly comparable to in-situ measurements at depth due to the vertical structure of salinity in the upper ocean associated with complex processes related to fresh water fluxes and ocean-atmosphere exchange. At L-Band in foam-free conditions, the emissive ocean surface layer is

~1cm deep (when foam is present, emissions may emanate from a layer >5 cm thick (Anguelova and Gaiser, 2011)), while the upper measurements performed by most in-situ devices (such as Argo floats, thermosalinograph onboard ships, or moorings networks) are in the depth range of 1 to 20 m. Furthermore, L-band satellite measurements are integrated over a large spatial footprint, from ~40 km to more than 100 km, which poses obvious representativity issues when compared to point samples from Argo floats or transects from ships. Hence, significant differences between satellite SSS compared to in-situ salinity have been observed with mean vertical differences larger than 0.1 in the Pacific, Atlantic, and Indian Oceans coinciding with the average position of the inter-tropical convergence zone (ITCZ). These issues have a strong impact when using in situ data for validation and vicarious calibration of satellite SSS products and must be managed with care in these areas of potentially significant vertical salinity stratification.

However, obtaining high vertical resolution measurements in the upper few meters of the ocean is still particularly challenging – even when using all available in-situ data sources. The study of the stratification of the upper ocean is the subject of dedicated experiments and its quantification via air-sea coupling modelling is still an active domain of research (e.g. (Drushka et al., 2019) and references herein).

In the open ocean, the uncertainty of the SMOS (Soil Moisture and Ocean Salinity), Aquarius and SMAP (Soil Moisture Active Passive) satellite SSS averaged over the GODAE scales is now estimated to be on the order of 0.2 (Reul et al., 2020; Vinogradova et al., 2019). Most recent SMOS processing largely reduces systematic errors in the vicinity of the coast and in areas polluted by radio frequency interferences (RFI) so that SMOS SSS is often very close to SMAP SSS, while SMAP data are less polluted than SMOS in these areas because of advanced RFI filtering capabilities (e.g. (Akhil et al., 2020; Fournier and Lee, 2021)).

Existing satellite SSS are capable of resolving large mesoscale and frontal SSS variability (spatial scale of 50-500 kms and temporal scale of 10-100 days) (e.g (Hasson et al., 2019; Huang et al., 2021; Kolodziejczyk et al., 2021; Lin, 2019; Melnichenko et al., 2021; Olivier et al., 2020)). These scales play an important role in the mixing and exchanges of water masses close to fronts, as a result of ocean circulation and atmospheric fluxes. At larger scales, ENSO events, which take place dominantly in the tropics, have serious climatic repercussions at planetary scale and are the main source of climatic variability at interannual scale with important consequences in many areas (agriculture, marine ecosystems, health…). Upper ocean salinity plays an active role in ENSO behavior (Zhu et al., 2014) and monitoring ENSO phases via dedicated SSS-based climate indexes (Qu and Yu, 2014) is useful to complement existing SST-based indexes and to better understand air-sea interaction processes during ENSO. There is furthermore some recent evidence that SSS provides also additional forecast skill for ENSO prediction (Hackert et al., 2020). Given the scientific advances made

possible by satellite-based SSS, the redefinition of the observation strategy in the tropical Pacific Ocean (Cravatte, 2016) and in the tropical Atlantic ocean (Foltz et al., 2019) underlined the need to pursue SSS satellite measurements.

Variations of precipitations above continents lead to variations of river discharges (Amazon/Orinoco, Congo, Niger, Mississippi) which, together with ocean circulation, lead to a large SSS variability in river plumes which have been well observed and documented by SMOS, Aquarius and SMAP measurements in the tropics (e.g. (Akhil et al., 2020; Fournier et al., 2016; Houndegnonto et al., 2021; Reverdin et al., 2021) and references herein).

It is estimated today that the active role of SSS on the dynamics of the surface layers of the ocean can lead to SSS feedbacks on the water cycle. Prior to the SSS satellite measurements, it had been suggested that in some tropical areas, the development of barrier layers could intensify the water cycle (e.g. (Shenoi et al., 2002)); under tropical cyclones, it would limit vertical mixing and hence cooling of the ocean surface which influences the development of the cyclones themselves (e.g. (Sengupta et al., 2008)). These processes have clearly been evidenced in SMOS and SMAP data analysis (Balaguru et al., 2020; Reul et al., 2021). These SSS feedbacks on climate are of increasing importance for climate studies.

Given the dependencies between salinity and carbonate properties of seawater, satellite SSS provides a means to better understand and constrain the spatio-temporal variability of the air-sea CO_2 exchanges, related to freshwater fluxes, and in particular the impact of precipitation (Brown et al., 2015; Ho and Schanze, 2020) and river plumes (Ibánhez et al., 2017; Lefèvre et al., 2014), as well as the total alkalinity and pH (Fine et al., 2017; Land et al., 2015; Salisbury et al., 2015).

The goal of the European Space Agency (ESA) Climate Change Initiative Sea Surface Salinity (CCI+SSS) project is to optimize satellite SSS time series by merging satellite SSS acquired by various instruments. For the first time, SMOS, Aquarius and SMAP measurements are combined to produce Level 4 (L4) gridded multi-mission estimates of SSS. Such a combination reduces the noise of satellite SSS fields owing to better sampling, and improve the spatial resolution of large mesoscale SSS features. Examples of the derived merged SSS L4 maps are illustrated in Figure 1 during a period with SMOS data-only, a period with SMOS plus Aquarius and a period with SMOS plus SMAP SSS measurements.

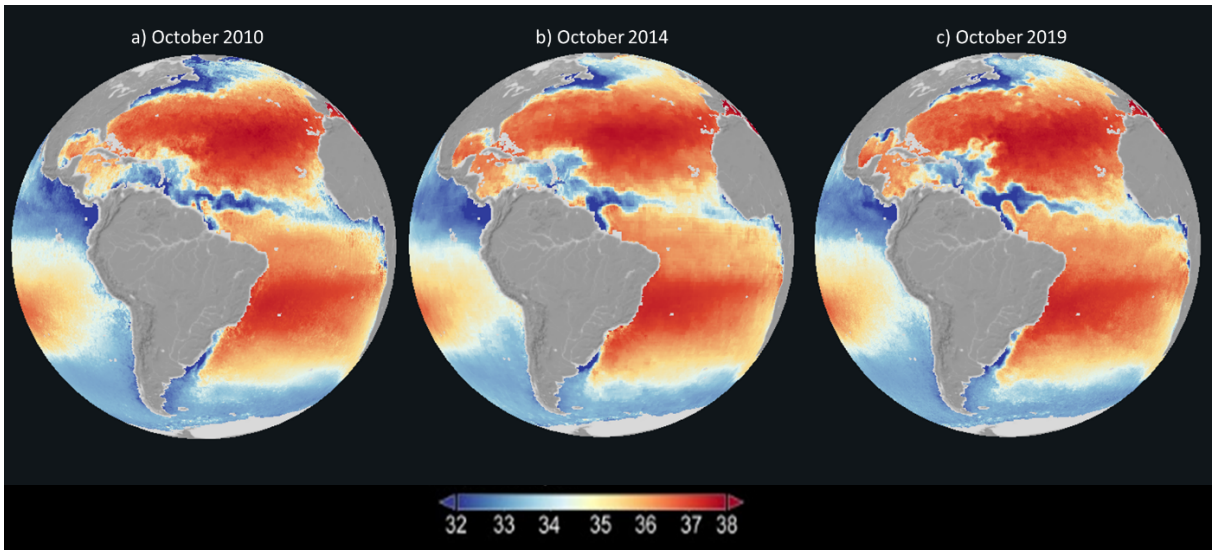

Figure 1: Example of CCI L4 satellite SSS fields in October a) 2010 (SMOS only period), b) 2014 (SMOS and Aquarius period) and c) 2019 (SMOS and SMAP period). (CCI monthly maps from the ESA Climate from Space website https://cfs.climate.esa.int)

The objective of this paper is (1) to review the user needs for SSS fields as expressed by the ocean and climate scientific community that guided the definition of CCI L4 SSS product characteristics; (2) to describe data and methods employed to build the CCI L4 SSS time series; (3) to analyze the resulting fields, and their validity; (4) to review and discuss the strength of satellite merged SSS, the remaining caveats and propose research avenues to solve or mitigate them.

2 SSS data requirements for ocean and climate studies

To create an SSS data set that satisfies the needs of climate users, both modeller and Earth-observing scientists groups, users of satellite SSS data were consulted through various approaches: personally, via e-mail, mailing lists, or at meetings. They were invited to participate in web surveys and to specify their requirements for satellite SSS data (see details of participating countries in supporting information S1). In our survey, we asked specific questions to find out the user's priorities (typically higher resolution or improved uncertainty estimates).

The survey (available on https://forms.gle/BVDroYrNpVvpxFJu9) gathered 54 answers. The majority of users require global spatial coverage and a temporal coverage from at least 9 years. The resolution requirements vary according to the studied phenomena. About 33% of respondents' want data with a temporal resolution of 1-3 days, while for 35% (28%) of the respondents' weekly (monthly) data are sufficient (Figure 2a). In terms of spatial resolution, 39% of the respondents want data in a 0.25° spatial grid, with 28% looking for 1° spatial grids (Figure 2b). The majority of respondents would prefer a data product with high

spatial and temporal resolution (weekly, 0.25°) on a regular latitude longitude grid. Interestingly, a majority of users would prefer a product with high temporal and spatial resolution and a lower accuracy rather than working with a product with high accuracy but lower resolution (Figure 2c). It was also found that the participants are aware of the data set limitations and have realistic expectations.

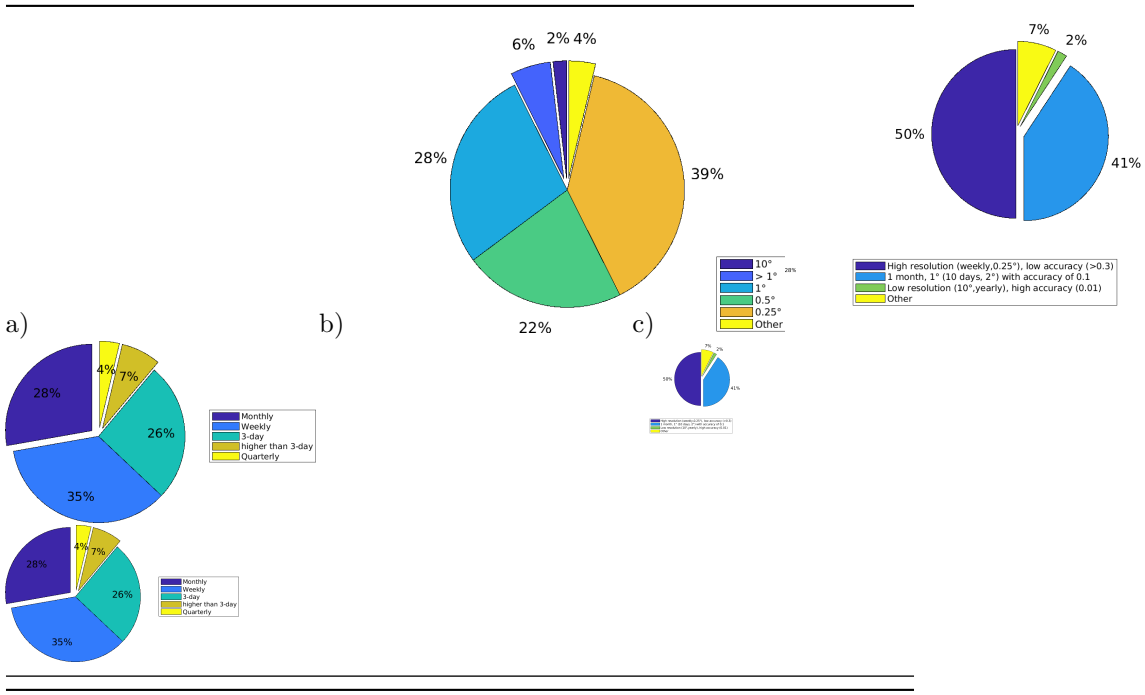

Figure 2: Percentage of required (a) temporal and (b) spatial resolution. c) Preferred SSS product based on the users spatial and temporal resolution needs.

According to the survey, data should be combined to overcome the weaknesses of individual datasets. 50% prefer a combination of satellite and in-situ measurements, whereas 39% require the combination of data from different satellite sensors. However, in the CCI L4 SSS products described here, information from in-situ measurements was restricted to a minimum in order to work with measurements having homogeneous spatio-temporal resolution and sampling. By making available the multiple-sensor datasets on different spatial-temporal grids, the needs of different users can be met. The most common requirement is for L4 data (43%), directly followed by requirements for L3 (37%). Some potential users, mainly modellers or scientists investigating rapid SSS changes, require L2 (20%). L3 and L2 data are already available from the original data centres (see section 3.2). L2 and L3 datasets including the CCI+SSS systematic corrections are kept as an internal CCI+SSS product.

Uncertainty information for each SSS grid point has to be fully characterized, including random noise and systematic uncertainties of the applied adjustments. Information about bias (systematic uncertainty) correction is most commonly required by respondents. 50% of respondents want to have flags for each/selected quality control checks, which is not possible for L3 or L4 datasets which are already binned. Therefore, quality information is needed for each SSS value that is simple to use, such as good/bad flag or the probability that a value is good/bad. 46% of the respondents would prefer such a solution for quality information. Participants also indicated how important a detailed documentation is.

User Requirement Survey results show the importance of contacting users and promote communication between the users and potential users of CCI L4 SSS fields. Users will be contacted regularly to refine requirements, to check the satisfaction with the CCI L4 SSS product. The recommendations regarding resolution, format, quality and additional information derived from the user consultation are summarized in the User Requirement Document (URD available on https://climate.esa.int/en/projects/sea-surface-salinity/key-documents/).

3 Data and Methods used for the generation of the CCI L4 SSS data set

The merging of the three existing satellite data sets is performed after standardizing the error estimation by using self-consistency criteria: by comparing SSS acquired at the same time by different sensors, we derive systematic and random uncertainties on SSS from each satellite mission. They are used to correct individual SSS before merging and to estimate final uncertainty on level 4 (L4) SSS. Two kinds of systematic uncertainties are corrected: a static bias which is associated to land-sea contamination, and sometimes to permanent radio frequency interferences (RFI), and a seasonal bias with a latitudinal dependency. The amplitude of these biases depends strongly on the sensor passes (ascending or descending), on the satellite pixel location on Earth, and, on the acquisition geometry (e.g., beam number (for Aquarius), across-swath position in the field of view (for SMOS), aft or fore view acquisition (for SMAP)).

The CCI+SSS algorithm is summarized in Figure 3. It is described in detail below after recalling the rationale behind the methodology we have followed and after describing the input data.

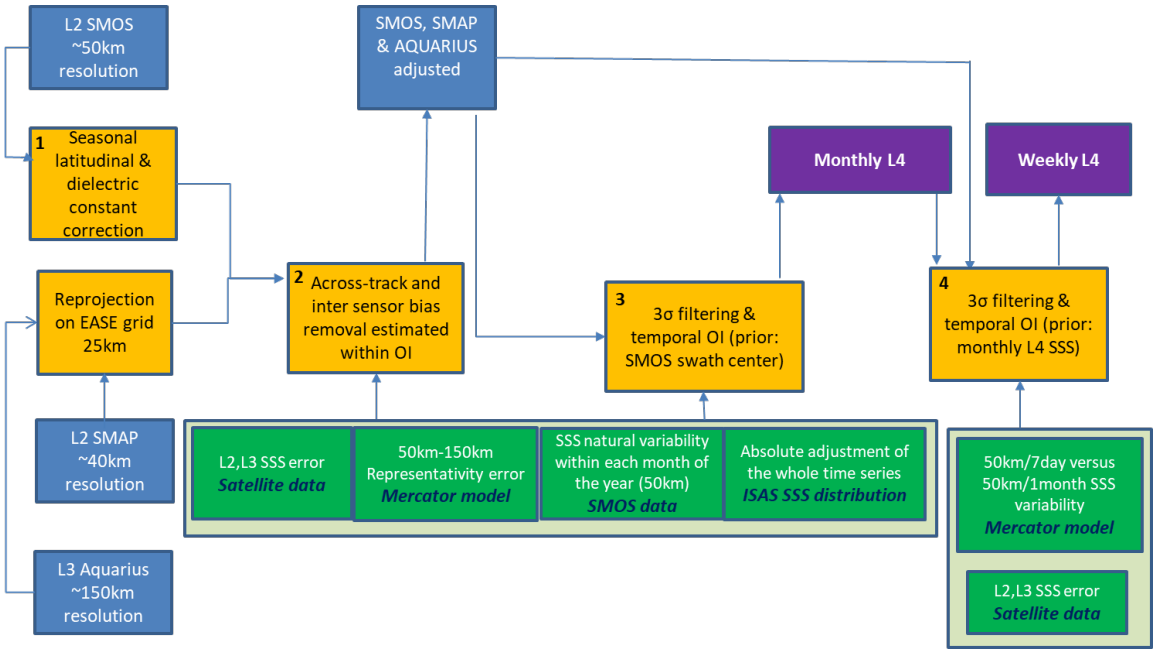

Figure 3: Schema of the CCI+SSS merging methodology. Satellite SSS data are indicated in light blue boxes, additional input information is in green boxes (origin of this information in bold black), processing steps are in yellow boxes and output CCI+SSS data are in violet boxes.

1.

2.

3. (a) Rationale of the methodology

- The systematic correction exploits as much information as possible from the data. SSS that seem to be affected by various contaminations (coastal, RFI, galactic, solar, etc.) are kept. It is considered that these effects can, to some extent, be corrected a posteriori.
- The self-consistency of the measurements (averaged in a monthly time window) over the whole time period, and considering the natural variability of the SSS expected in this time window, allows the inter-sensor systematic differences to be corrected relative to each other, similar to what is described in (Boutin et al., 2018).
- A temporal self-consistency criterion is considered in the algorithms. Actually, a spatial adjustment of the SSS according to a certain reference (e.g., SSS climatology) could affect spatial and temporal dynamics and could remove some of the interannual

signals and mesoscale signatures. We, therefore, assume that land sea contamination biases are constant over time, a reasonable assumption given that temporal variations in Tb on land are generally an order of magnitude smaller than the contrast between Tb on land and at sea. These biases can be corrected without affecting geophysical SSS dynamics. In practice, the SSS correction/estimation is done on a grid node by grid node basis, considering the self-consistency of the SSS measured by the different sensors under various geometries (Kolodziejczyk et al., 2016). To correct seasonal latitudinal biases, a relative correction is also applied, similar to what is described in (Boutin et al., 2018). It applies to all basins and should not affect the interannual dynamics.

- The various corrections are relative. As a result, SSS anomalies are available at the end of the OI processing. These anomalies are then vicariously calibrated against an absolute reference. This adjustment is a time-independent shift aiming to maintain the temporal dynamics of the SSS.
- In the settings of the various processing parameters (correlation time period, a priori variability), slowly-evolving time fluctuations are estimated to reduce uncertainties as much as possible. This is why the CCI L4 SSS products are split into two subproducts: a monthly product and a weekly product.

1. Input Satellite Data

The main characteristics of L-band radiometric satellite missions enabling global SSS measurements are summarized in **Table 1**.

Below, we report the information relevant for CCI+SSS version 2 dataset. Information relevant for CCI+SSS version 1 is provided in supporting information S2 and S3. We consider the longest SMOS, SMAP, and Aquarius SSS time series available at the time of the development of each CCI L4 SSS data set. We use the SSS data retrieved with up-to-date algorithms (**Table 2**). SMOS data are level 2 products generated internally by the *Centre Aval de Traitement des Données SMOS* (CATDS), the so-called L2P products based on SMOS ESA L2 v622 algorithm (Arias and SMOS_Ocean_Expert_Support_Laboratories, 2016). SMAP v3 and Aquarius v5 SSS data are retrieved using (Meissner et al., 2018) algorithms. SMAP algorithm has been updated towards version 4 as described in Meissner et al. (2019) with improved land correction, sea-ice mask, ice flagging. SMAP and Aquarius SSS are reprojected on the SMOS CATDS spatial grid, the rectangular Equal-Area Scalable Earth grid (EASE 2.0) grid (Brodzik et al., 2012) at 625 km^2 surface resolution (called 25km EASE grid in the following), using a nearest neighbor criterion.

RFI and calibration stability are two main challenges to deal with before retrieving reliable SSS measurements, given the low signal-to-noise ratio of Tb

relative to salinity (0.5K per salinity unit at 20°C at nadir). Details about data processing for each satellite mission are given below.

Table 1. Missions characteristics

SMOS MISSION	**AQUARIUS MISSION**	**SMAP MISSION**
Mission Characteristics		
-L-band interferometry. 0°-~60° earth incidence angles -revisit times: 4 days -resolution: about 45 km -repeat sub-cycle: 18 days -see more in (Font et al., 2010; Y. Kerr et al., 2010)	-L-band real-aperture radiometer. 3 fixed beams at 28.7, 37.8, and 45.6° earth incidence angles -revisit times: 7 days -resolution: about 150 km -repeat cycle: 7 days -see more in (Lagerloef et al., 2008)	-L-band real-aperture radiometer. Conical scanning, 40° earth incidence angle -revisit times: 3 days -resolution: about 45 km -repeat cycle : 8 days -see more in (Piepmeier et al., 2017)
Vicarious calibration		
-Spatially constant and time-varying mean calibration: OTT: 10day mean differences in the south-east Pacific Ocean using World Ocean Atlas climatological SSS (Yin et al., 2013).	- Spatially constant and time-varying mean calibration: OTC: 7day mean differences over global ocean using Scripps Argo SSS (Meissner et al., 2018).	- Zonal calibration: emissive reflector correction to minimize orbital biases, estimated for each day of the year using Scripps Argo SSS. It is the same for all years (Meissner et al., 2019) - Spatially constant and time-varying mean calibration: OTC: 3day mean differences over global ocean using Hycom SSS (Meissner et al., 2019).
RFI filtering		
No specific RFI detection. Outlier detection performed in Level 2 processing.	Specific RFI detection (Le Vine and Matthaeis, 2014)	Specific RFI detection (Soldo et al., 2019)

Table 2. Satellite SSS products used to derive version 2 CCI L4 SSS fields.

Data coverage	[2010-2019]
SMOS SSS	L2P CATDS from ESA v622 algorithms (CATDS, 2017) with the following filterings: - Normalized of the retrieval, $_{N}^{*} <$ 3 - SSS random uncertainty, $E_{SSS\_L2}{}^{*} <$ 3 - center of the swath (+/-400 km) - pixels with small number of Tb outliers (level 2 fg_outlier flag) - ice contamination: (level 2 Dg _suspect_ice=0) (This flag removes pixels in cold waters (SST<2°C) in which at least one Tb differs by more than 20K from modelled Tb. It is a very stringent filtering that is likely to be removed in future versions. - Pseudo-dielectric constant retrieved from SMOS (Acard) (Acard smos – Acard mod<2 and Acard>42), where Acard mod is Acard simulated with SSS and SST. This filtering allows removing moderate to strong RFI and ice contamination (see more in (Supply et al., 2020b)). - wind speed < 16 m/s - SSS > 2 & SSS<45
SMAP SSS	L2C v4.0 RemSS (Meissner et al., 2019) Flagging as recommended in the user guide. Reprojection on 25 km EASE grid using nearest neighbor criteria.
AQUARIUS SSS	L3 daily products (Ascending and Descending orbits separated) (Meissner et al., 2018) Nearest neighbor colocation applied to 25 km EASE grid pixels falling within a 1°x1° Aquarius pixel.

**defined as in (Boutin et al., 2018)*

SMOS, Aquarius and SMAP missions operate in a protected spectrum band (1400-1427 MHz) that is nevertheless known now to be vulnerable to numerous

RFI. Areas affected by RFI might experience data loss or result in inaccurate salinity retrieved values. To alleviate this situation, several strategies were set up to filter RFI contaminated measurements. SMOS, launched in 2009, was the first satellite with a radiometer operating in L-band, and it does not have any on-board hardware/software to filter RFI, so that RFI counteracting only relies on data post-acquisition processing. Filtering is significantly improved for SMAP (and to a least extent for Aquarius), as they are (were) equipped with on-board frequency/time-domain-based RFI filters but RFI still remains a major problem (e.g. (Kristensen et al., 2019)).

Over the ocean, SMOS data are contaminated by RFI emitted principally from land. They can induce positive or negative errors on the reconstructed brightness temperature. RFI impact is not limited to the location of the on-ground antenna causing the interference as it affects remote measurements as soon as the line of sight is between the instrument and the RFI source (Oliva et al., 2016). Due to the interferometer principle from a Y-shape antenna, the contamination is not circularly symmetric in SMOS images, but presents six main tails spreading from the RFI source. In the case of SMAP and Aquarius, the RFI contamination is different as both missions operate real-aperture radiometer and on-board data filtering with enhanced detection capabilities. For protection against RFI, Aquarius employs rapid sampling (10 milliseconds) and a "glitch" detection algorithm that looks for outliers among the samples. Samples identified as RFI are removed, and the remainder is averaged to produce an RFI-free signal for the salinity retrieval algorithm. The RFI detection algorithm appears to work well over the ocean with modest rates for false alarms (5%) and missed detection, however RFI are still detected in Aquarius (Le Vine and Matthaeis, 2014). SMAP takes a multidomain approach to RFI mitigation by utilizing an innovative onboard digital detector backend with digital signal processing algorithms to characterize the time, frequency, polarization, and statistical properties of the received signals. Almost 1000 times more measurements than what is conventionally necessary are collected to enable the ground processing algorithm to detect and remove part of the signal bandwidth affected by RFIs. This algorithm is rather efficient, even though some disturbances still remain and bandwidth reduction is expected to lead to increased noise (Soldo et al., 2019).

Onboard calibration and correction for parasite effects (e.g., solar perturbations) in present processing do not allow to reach enough Tb stability and accuracy to cope with the requirements of SSS remote sensing. As a consequence, before retrieving SSS, vicarious calibrations are applied for removing spatially constant but time-varying biases in the measured minus expected radiometric signal. For SMOS, the so-called Ocean Target Transformation (OTT) consists of 10-day mean differences estimated in the south-east Pacific Ocean, between 5°S and 45°S, a region almost unaffected by RFIs (Yin et al., 2013). For Aquarius and SMAP the Ocean Target Calibration, OTC consists in 7-day mean differences at global scale (Meissner et al., 2018). An additional zonal-seasonal varying correction for the antenna emissivity is applied to SMAP before applying the

OTC. The SSS references taken for each of these corrections come from either a climatology, an ocean model (Hycom) or an Argo-derived field, the choice being partly driven by the reference product availability with respect to production temporal constraints.

Auxiliary geophysical information is necessary to initialize the SSS retrieval. Wind, SST and atmospheric parameters are taken from European Center for Medium Weather Forecast (ECMWF) Integrated Forecast System (IFS) in the case of SMOS. In the case of Aquarius and SMAP, atmospheric parameters are taken from NCEP (National Centers for Environmental Prediction) GDAS (General Data Assimilation System) and SST is from the Canadian Meteorological Center (CMC). In the future, the Copernicus Microwave Imaging Radiometer (CIMR) (Donlon, 2020)) will provide L-band measurements together with higher frequency data that are sensitive to SST (C-band), and surface roughness (K-band) allowing a more precise initialization of SSS retrieval.

1. Auxiliary information

   (a) ISAS

Monthly gridded fields of salinity derived from in-situ measurements are obtained from the ISAS (In-situ Analysis System) v6 algorithm, an optimal interpolation tool (Bretherton et al., 1976) developed for the synthesis of the Argo global dataset (Gaillard et al., 2016). We use the ISAS fields reconstructed at 5 m depth on a half degree horizontal grid. The statistical distribution of monthly ISAS SSS in each grid point is used to adjust the long-term absolute reference of the CCI L4 SSS corrected fields (see section 3.4.2.1). ISAS 2011-2016 latitudinal profiles have also been qualitatively used as an indicator of the SMOS SSS reference across swath location (see Appendix A1 of Boutin et al. (2018)).

1. Mercator model simulations

We derive SSS variability at various spatio-temporal scale that are not resolved from satellite missions using Mercator model higher spatio-temporal resolution analysis. We use the daily salinity fields at 0.5 m depth between 2011 and 2014 provided by the Global Ocean Reanalysis Products GLOBAL-REANALYSIS-PHY-001-030, generated by an eddy resolving (1/12°) global ocean model constrained by assimilation of satellite sea level anomalies, SST, sea ice concentration (but excluding the satellite SSS measurements), of in-situ temperature and salinity vertical profiles and constrained by climatological runoffs, that will be called GLORYS in the following. It describes the spatio-temporal evolution of tri-dimensional thermodynamic variables (T, S), tri-dimensional dynamic variables (U, V), sea surface height and sea-ice features (concentration, thickness and horizontal velocity). More information about this product can be found on https://resources.marine.copernicus.eu/?option=com_csw&view=details&product_id=GLOBAL_REANALY

1. Methodology

Monthly and weekly maps of SSS are derived from the three satellite missions using a temporal optimal interpolation (OI). We do not apply any spatial smooth-

ing so that the spatial resolution of each level 4 SSS is 50 x 50 km^2. They are re-sampled to a 25 km EASE grid. We correct for systematic differences between the SSS from the various satellite missions acquired with different geometry as will be described below. We provide an uncertainty associated to the CCI L4 SSS product.

In the following, we describe the methodologies we follow to derive level 4 SSS fields, successively including:

- the optimal interpolation method,

- the characterization of the uncertainties on level 2 SSS derived from each satellite mission, linked to observational errors (Vinogradova et al., 2019), (with a covariance matrix denoted Cd in the following),

- the quantification of the SSS natural variability involved in:

- the representativity uncertainty, also called sampling uncertainty (Vinogradova et al., 2019), which originates from the different samplings of the various sensors, (with a covariance matrix denoted Cr in the following),

- the spatio-temporal variability relative to a mean value used to adjust the OI estimate (covariance matrix denoted C2 in the following).

We explain below the strategy adopted in CCI+SSS version 2. Differences between methodologies applied in CCI+SSS version 1 and 2 are reported in supplementary material.

1. Generation of level 4 fields:

In order to estimate SSS at a given time, the algorithm is using an optimal interpolation. This interpolation is applied grid node per grid node, without spatial smoothing. Indeed, we want to preserve the spatial and temporal dynamics of the SSS and to avoid a spatial catch-up made to monthly reference climatological fields which might remove or attenuate important interannual and/or large mesoscale variations.

To better understand the process, let's consider SSSobs observations from a single sensor. First, systematic uncertainties are ignored. To estimate an SSS time series of spatial resolution R1 and temporal resolution T1, knowing that the observed data SSSobs are at spatial resolution r1 and temporal resolution t1, the cost function to be minimized is written (as a scalar product <XY>):

$$C(SSS) = < SSSobs - SSS | \mathrm{Ct}^{-1} \cdot (SSSobs - SSS) > + < SSS - SSSprior | \mathrm{C2}^{-1} \cdot (SSS - SSSprior) > \quad (1)$$

uncertainty Cr (section 3.4.4) added to take into account the difference in reso-

lution of fields (R1;T1) and (r1;t1):

Ct=Cd+Cr

This covariance is seasonal and specific to each grid node.

C2 corresponds to the variability of the field with the spatio-resolution (R1;T1) relative to the SSSprior field. Again, this variability is seasonal and different for each grid node.

However, each sensor must be considered independently in the cost function considering the space and time resolution of each product. In the case where we estimate the monthly SSS field from the three sensors SMOS, SMAP, and Aquarius, we therefore have:

$C(SSS)=\langle SSSobs\_smos\text{-}SSSCt\_smos^{-1} \cdot (SSSobs\_smos\text{-}SSS)\rangle +$

$\langle SSSobs\_smap\text{-}SSSCt\_smap^{-1} \cdot (SSSobs\_smap\text{-}SSS)\rangle +$

$\langle SSSobs\_aqua\text{-}SSSCt\_aqua^{-1} \cdot (SSSobs\_aqua\text{-}SSS)\rangle +$

$\langle SSS\text{-}SSSpriorC2^{-1} \cdot (SSS\text{-}SSSprior)\rangle$

In the SMOS and SMAP covariance uncertainty, we neglect the representativity uncertainty that corresponds to the transition from acquisition time (about one second) to monthly resolution (30 days), as, in the majority of cases, SMOS and SMAP observational uncertainty are much larger than representativity uncertainty. For Aquarius, which has much smaller observational uncertainty, the algorithm takes into account representativity uncertainty.

Finally, the cost function also contains estimation of systematic uncertainty, also called biases. For each type of acquisition, a different relative bias is considered. Only a constant bias over the whole time series is taken into account, the latitudinal bias being corrected beforehand (section 3.4.2.1). An a posteriori uncertainty term, corresponding to a L4 SSS uncertainty, is also derived.

A detailed description of the algorithm is provided in the supporting information S4.

The methodology used to estimate observational random uncertainty, representativity uncertainty and SSS variability considered in the algorithm is described in the following sections. An example of climatological monthly SSS variability, the dominant term among the representativeness uncertainty and the variabilities between the several spatio-temporal scales involved in the OI, is illustrated on **Figure 4** for the month of August. The main regions of high variability are consistent with expectations i.e. river outflow regions (Amazon, Congo, Mississippi, Ganges) and Gulf Stream variability. Other examples of representativeness uncertainty and the variabilities used in the OI are provided in supporting information S5.

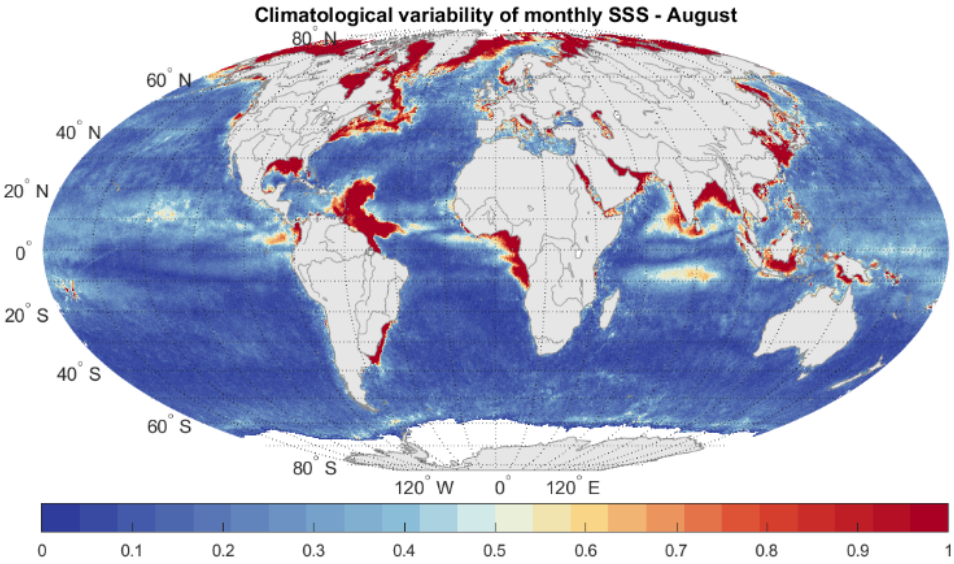

Figure 4: Climatological map of monthly SSS variability in August (deviation to the SSS averaged over the whole period), that is considered in the optimal interpolation.

1. Observational SSS uncertainty:

The issues affecting the retrieved level 2 SSS uncertainty are of different origins, which include:

- Poorly modeled instrumental effects (solar influence, land contamination of the instrument side lobes, absolute calibration …),
- Radiometric noise,
- Flaws in the radiative transfer model (e.g. deficiencies in dielectric constant modeling in cold areas, rough sea surface emission and scattering of galactic and solar radiation…),
- Uncertainty in auxiliary geophysical data used as priors in the retrieval algorithms (wind speed, SST…),
- Measurement contamination by spurious effects (e.g. RFI).

The simplest way to qualify these aspects is to associate them with two statistical indicators, a systematic component and a random component. The strategy for determining these uncertainties is summarized in **Table 3** and detailed below.

Table 3: Strategy for uncertainty characterizations.

Random uncertainty estimation	Self-consistency approach. Random uncertainty modelling according to t
Systematic uncertainty estimation	Self-consistency approach (ISAS SSS distribution only used for whole pe
Latitudinal seasonal correction	SMOS: Self-consistency approach: in each pixel, use reference SSS from

Random uncertainty estimation	Self-consistency approach. Random uncertainty modelling according to t
SSS correction at low SST	SMOS: (Dinnat et al., 2019)
Random uncertainty propagation	Least square method.

1. Systematic uncertainty of satellite SSS measurements:

We first consider systematic differences depending on SST. Dinnat et al. (2019) found systematic errors of SMOS SSS as a function of SST that are attributed to deficiencies of the Klein and Swift (1977) dielectric constant model at extreme SST values. This leads us to adjust SMOS SSS with a polynomial SST function (box 1 of **Figure 3**). We derive these specific SMOS data adjustment from comparisons between Aquarius SSS (retrieved with similar dielectric constant model and atmospheric model than SMOS processing models), and Argo SSS (blue dotted curve of Figure 16 of (Dinnat et al., 2019)).

No correction depending on SST is applied for SMAP and Aquarius SSS as in their L2 respective processing chains (Meissner et al., 2018), the sea surface roughness emission contribution already includes an empirical SST adjustment.

We then remove main remaining systematic uncertainty following the methodology described in (Boutin et al., 2018) but applied to different sensors. It considers zonal seasonal varying biases (e.g. those linked to solar or galactic effects), as well as a constant bias over time which varies as a function of the location on the globe, the instrument and the geometry of observation (e.g. land-sea contamination):

$SSS_{obs}(t, \ , \ ,X, x_{orb})=SSS_{ref}(\ , \ ) + SSS_{rel}(t, \ , \ , X, x_{orb}) - b_c(\ , \ ,X, x_{orb}) - b_{lat}(\ ,X,x_{orb},m)$ (2)

where SSS_{obs} is the observed SSS, t is the time of the measurement, , and , are respectively the latitude and the longitude of the considered pixel over the ocean, X corresponds to a geometry of observation, x_{orb} indicating the satellite orbit direction (ascending or descending); b_c is a correction constant in time, b_{lat} is a zonal correction that varies seasonally as a function of the month, m. b_{lat} and b_c are relative corrections with respect to an arbitrary reference SSS constant over time, SSS_{ref}. The residuals of SSS_{obs} - SSS_{ref} + b_c + b_{lat} correspond to the relative variations of SSS with respect to SSS_{ref} and are called SSS_{rel} (see example on **Figure 5**ab). b_{lat} and b_c are derived through a least square minimization approach, and through a series of iterations. The arbitrary reference is taken as the mean of all SSS. At the end of the correction process, the whole corrected SSS time series are adjusted with a time-invariant shift derived from intercomparison of a quantile of corrected SSS and of ISAS SSS (**Figure 5**d). In regions with low SSS variability the 50% quantile (median) is considered, and it is increased up to 80% in regions with high SSS variability, where SSS statistical distribution is skewed towards low values which are not well represented in ISAS fields, due to the Argo undersampling and ISAS smoothing.

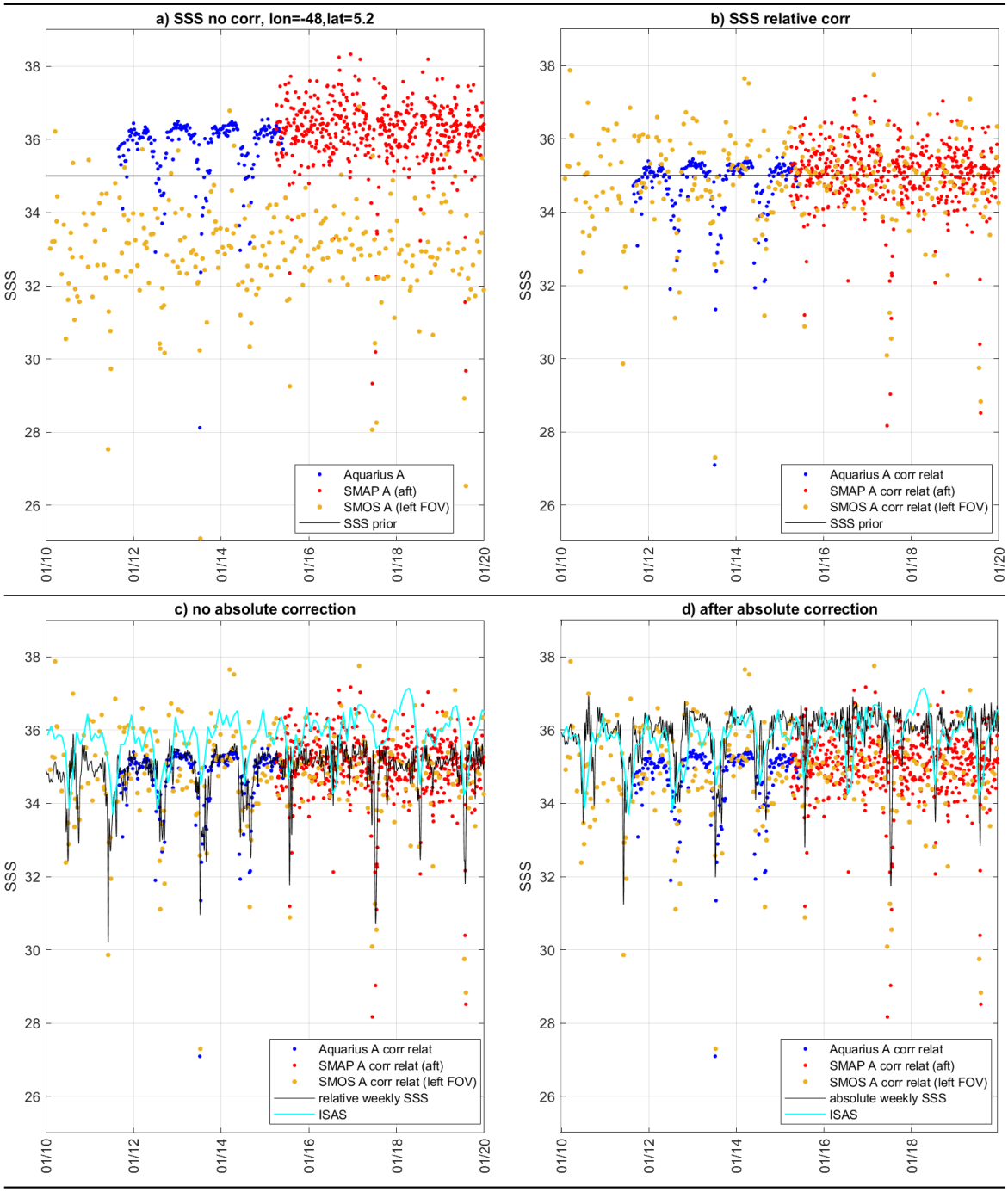

Figure 5: Principle of the self-consistency approach. Example of a grid point

near the Amazon plume (48°W, 5.2°N) affected by land sea contamination, seen under various satellite geometry during ascending orbits (SMOS L2 SSS, left hand side of the FOV, green points; SMAP L2 SSS, aft antenna, red points; Aquarius L3 daily SSS, blue points). a) Satellite SSS before correction (SSS_{obs}) and SSS_{ref} (black line) ; b) Satellite SSS after relative adjustment (SSS_{rel}+SSS_{ref}) and SSS_{ref} (black line); c) Satellite SSS after relative adjustment (SSS_{rel}+SSS_{ref}), weekly OI relative SSS (black) and ISAS SSS (light blue); d) Same as c) but after absolute calibration of the weekly OI SSS by adjusting the 80% quantile of the weekly OI SSS statistical distribution to that of the ISAS SSS.

b_{lat}, is only considered for SMOS data (box 1 of Figure 3) with X representing the pixel location across the swath. We do not apply seasonal latitudinal correction to SMAP SSS as the reflector emissivity correction (Table 1) already ensures zonal seasonal consistency with Argo. Seasonal latitudinal biases are neglected as a first step for Aquarius SSS because they are smaller than SMOS ones. They could however be considered in future CCI+SSS versions as Kao et al. (2018) and Meissner et al. (2018) found zonal seasonal SSS systematic differences with respect to Argo SSS or between ascending and descending passes that can reach +/-0.2. b_c is considered for all sensors. X corresponds to fore or aft acquisition for SMAP, to across swath location for SMOS and do not vary for Aquarius. Actually, for a given x_{orb}, a pixel at a (,) location is always seen by the same Aquarius antenna; possible biases between the three Aquarius antennas acquisitions are corrected by b_c estimated in different pixels. The largest b_c occurs in the vicinity of land masses for SMOS data.

1. Random uncertainties of satellite SSS measurements:

The SMOS processing provides a 'theoretical' random error, E_{SSS_L2}, derived from the Jacobian of Tb relative to SSS and auxiliary parameters, the expected radiometric noise, the expected random errors on auxiliary parameters and on radiative transfer model. A more realistic estimate of the SSS random uncertainty, is obtained by multiplying E_{SSS_L2} by the normalized of the Bayesian retrieval, $_N$ (Boutin et al., 2018).

For SMAP and Aquarius SSS, we derive random uncertainties from self-consistency analyses of the observed SSS as a function of SST. We check that they correspond to a realistic radiometric noise given the SST dependency of Tb derivative with respect to SSS (Yueh et al., 2001). A theoretical uncertainty is derived that is used for our analysis.

For SMAP, we derive empirical uncertainties by comparing collocated retrieved SSS between fore and aft acquisitions. We computed the standard deviation, std, of the difference which should be an estimator of the SSS random uncertainty multiplied by $\sqrt{2}$ (assuming that the random uncertainty are the same for aft and fore acquisitions). The std of the difference is very close to a modelled uncertainty with a 0.45K radiometric noise.

For Aquarius, the random uncertainties are derived from comparisons of the

Aquarius SSS at time t with the Aquarius SSS at time t + 7 days due to the 7-day periodicity of the satellite orbit. For that, we assume that SSS in the open ocean does not change significantly in 7 days, so that the std of the difference relates to the random error (multiplied by $\sqrt{2}$). A fit to the observed random errors is derived as a function of SST (see supporting information S6).

We check the reasonable behavior of estimated random uncertainties, SSS, by considering the statistical distribution of the centered reduced SSS, namely, SSSc:

$$SSSc = \frac{SSSobs - SSSref}{\mathrm{SSS}} \#(\ SEQ \ quation \ \backslash * \ ARABIC \ 3)$$

Where SSSobs is the retrieved SSS possibly corrected from systematic errors and SSSref is a reference SSS. We find that the distribution of SSSc is most often close to a Gaussian law with a std equal to 1 over the open ocean at distances further than 800 km from the coast. Closer to the coast, std($SSSc$) deviates from 1. Hence, we estimate multiplicative factors, f(dcoast), to be applied to SSS, for each instrument independently. Since part of this difference can be associated to the variability of the salinity, we quantify std($SSSc$) in grid nodes with low spatio-temporal SSS variability, lower than 0.2, as derived from each instrument rmsd. We then adjust f(dcoast) so that robust std (median absolute deviation divided by 0.67) of SSSc becomes close to 1 (see supporting information S6).

1. SSS variability:

SSS variability is considered at two temporal scales in the OI (Cm matrix):

- the variability of monthly averaged SSS with respect to the original SSS time series averaged in each pixel. It is used to derive the relative biases between the various dwell lines and to estimate the monthly SSS;

- the variability of SSS at 50km/7days relative to SSS at 50km/1month resolution, that is used to estimate weekly SSS, taking monthly SSS as priors.

Monthly SSS variability with respect to the SSS average over the whole time period is estimated on each grid node and for each month of the year as the RMSD between monthly SSS for the considered month and the SSS average over all months, and for all years. Hence the variability is seasonal and the SSS is allowed to fluctuate more or less around its mean value with the seasons. To remain as coherent as possible with respect to the variability sampled by the satellite measurements, we prefer to avoid estimating it from the Mercator model. Instead, we estimate it recursively from satellite SSS fields as follows.

In a first step, we estimate this variability from the SMOS filtered SSS fields in regions which are not strongly contaminated by errors (low to middle latitudes, excluding RFI contaminated areas). In regions where SMOS SSS are very noisy (such as in RFI contaminated areas e.g. close to Fiji island or in the Bay of Biscay, we artificially set a low variability; at very high latitudes, we consider ISAS SSS variability increased by a factor of 2 in order to leave the possibility of

unexpected fluctuations). These fields are then used to provide a first estimate of CCI L4 SSS fields. The monthly variability is then derived from these first SSS estimates (see Figure 4 and supporting information S5).

Estimates of the variance of weekly fluctuations relative to the monthly averaged fields are derived from Mercator model simulated SSS. Since river discharges used in Mercator model are based on climatological river runoff information, temporal and spatial variations in river plumes are not properly considered and may be underestimated. We therefore take an estimate for this variability defined by twice the RMSD between 50 x 50 km^2 daily and 50 x 50 km^2 30-day mean SSS for each month, obtained from the Mercator fields at $1/12^{th}$ of a degree resolution and we then smooth this variability over a space scale of 200 km (see supporting information S6).

1. Representativity uncertainties:

In order to estimate the Cr matrix used in the cost function, we estimate a representativity uncertainty for Aquarius, corresponding to the SSS variability in between the spatio-temporal scale resolved by Aquarius and by the CCI fields. The aim is to increase the uncertainty associated with the Aquarius data by a representativity uncertainty that can be calculated from a model such as Mercator. We estimate that uncertainty as the standard deviation of the SSS between fields smoothed over 150 x 150 km^2 with respect to 50 x 50 km^2 averages. This information is calculated off-line using Mercator model outputs. This representativity uncertainty depends on the month and dynamics of the SSS field (see supporting information S7). Indeed, in some parts of the ocean, SSS does not vary over large distances and durations: in this case, the representativity uncertainty tends towards 0. Tests using this representativity uncertainty lead to too smoothed L4 SSS fields particularly in very variable areas near the coasts suggesting that the representativity uncertainty is not large enough. This might be due, among other reasons, to the spatial variability of the SSS not well reproduced by GLORYS simulations, especially given the limited 2011-2014 time period we considered, as well as to non-Gaussian distribution of the SSS not handled by our method. In order to bypass these artefacts and to keep small scale features detected by satellite data, possibly at the expense of an increased noise of the L4 fields, we proceed as for the weekly variability: the variability was spatially smoothed and doubled. This rather raw methodology should be revised in the future.

Representativity uncertainties are generally low (compared to observational uncertainties) for grid nodes in the open ocean but are large near river mouths, in rainy areas and in very dynamical regions (e.g. Gulf Stream).

Close to the coast and at the river mouths, these uncertainties are difficult to assess to a large extent because of the high interannual variability that limits the validity of the statistical approach. These uncertainties can be greater than 1 and becomes dominant in the error budget as they are larger than the SSS observational random uncertainties of original L2 satellite data.

1. Validation of CCI L4 SSS:

Systematic validations of CCI L4 SSS with respect to various in-situ SSS have been performed by the SMOS Pilot-Mission Exploitation Platform (PIMEP). The full PIMEP comparisons between weekly or monthly CCI+SSS fields and in-situ measurements are available on https://www.salinity-pimep.org/reports/mdb.html. We summarize in this paper the most striking results, by considering comparisons with in-situ data from Argo profilers, from Voluntary Observing Ships (VOS) and from Research Vessels (RV). We summarize below the caracteristics of each dataset and the methodology used to build the matchup data bases (MDB) with CCI L4 SSS.

1. Comparisons with Argo SSS:

Argo is a global array of almost 4,000 free-drifting profiling floats that measure temperature and salinity of the upper 2000 m of the ocean. This allows continuous monitoring of the upper ocean conditions, with all data being transmitted by the GTS and made publicly available within the 24 hours after collection. The array provides around 100,000 temperature/salinity profiles per year distributed over the global open ocean. Only Argo salinity and temperature float data with a quality flag set to 1 or 2 and data mode set to real time (RT), adjusted (A) or delayed mode (DM) are considered in Pi-MEP. Argo floats that may have problems with one or more sensors appearing in the grey list maintained at the Coriolis/GDACs are discarded. Furthermore, Pi-MEP provides an additional list of 1000 "suspicious" Argo salinity profiles that are also removed after visual inspection. The upper ocean salinity and temperature values recorded between 0 m and 10 m depth are considered as Argo sea surface salinities (SSS) and sea surface temperatures (SST). These data were collected and made freely available by the international Argo project and the national programs that contribute to it (ARGO, 2020).

The Argo Match-up Data Base (MDB) is produced from the previously described cleaned Argo dataset. For the monthly *(weekly)* CCI L4 SSS product, the match-up co-localization temporal window search radius is chosen to select the closest match-up both in time and space, within the spatio-temporal resolution of the satellite fields, i.e. within ± 7.5 *(0.5)* days around the central date of each satellite time step and within a spatial radius of 12.5 km around each satellite grid node center. If several satellite pixels are found to meet these criteria, the final satellite SSS match-up point is the closest in time from the in-situ data measurement date.

1. Comparisons with SSS collected by ship thermosalinograph:

Ship ThermoSalinoGraph (TSG) measurements are sampled at a few kilometres along ship transects, hence, reducing the spatial representativeness uncertainty in a satellite pixel with respect to Argo. These higher resolution 'validation' data are therefore very useful in very variable regions and in the vicinity of land. In this study, we have considered the GOSUD-RV and the LEGOS-DM datasets

located mostly at low to mid latitudes, which are very complementary to Argo in high SSS variability regions (**Figure 6**).

The TSG-GOSUD-Research-vessel dataset correspond to French research vessels, which have been collecting data since the early 2000 in contribution to the GOSUD program. The set of homogeneous instruments is permanently monitored and regularly calibrated. Water samples are taken on a daily basis by the crew and later analysed in the laboratory. The careful calibration and instrument maintenance, complemented with a rigorous adjustment on water samples lead to reach an accuracy of a few 10^{-2} in salinity. This delayed mode dataset (Kolodziejczyk et al., 2020) is updated annually and freely available on https://www.seanoe.org/data/00284/39475/ . Adjusted values when available and only collected TSG data that exhibit quality flags 1 or 2 were used.

The TSG-LEGOS-DM dataset are delayed mode data derived from voluntary observing ships collected, validated, archived, and made freely available by the French Sea Surface Salinity Observation Service (Alory et al., 2015). Adjusted values when available and only collected TSG data that exhibit quality flags=1 and 2 were used.

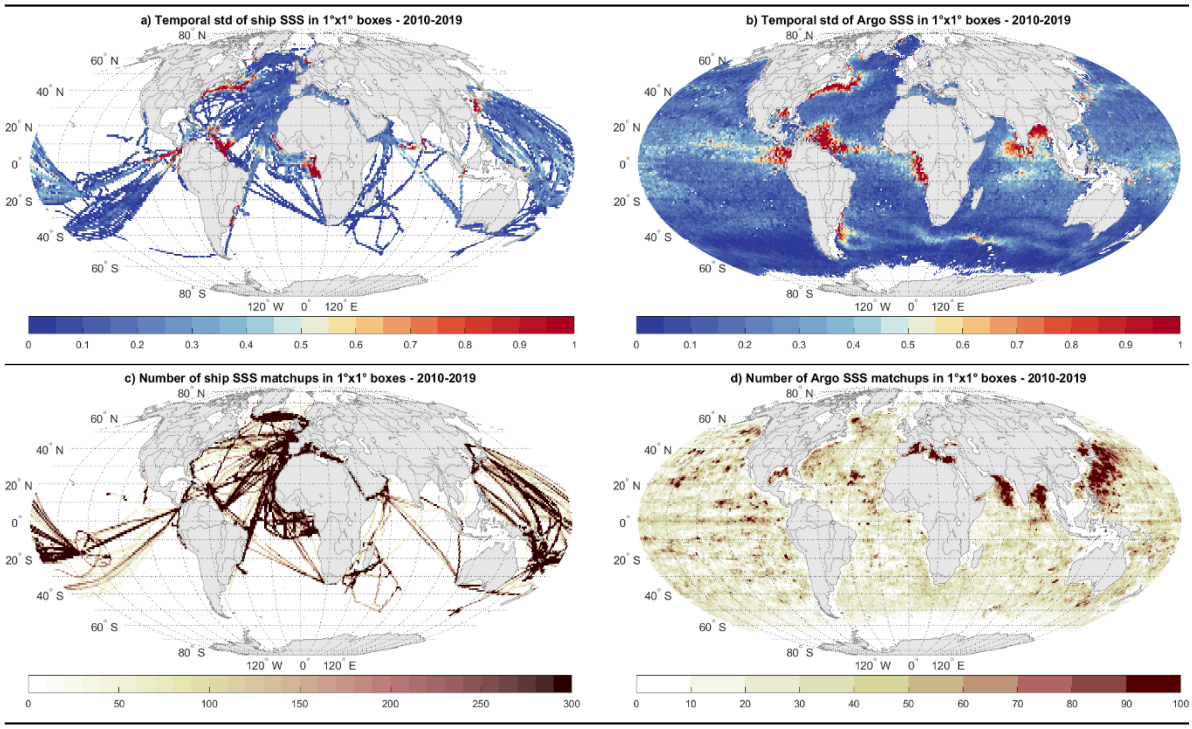

Figure 6: Temporal SSS Std, in spatial boxes of size 1∘x1∘ of ship TSG (LEGOS DM and GOSUD-Research-vessel) (a) and Argo (b) and Number of ship-CCI matchups (c) and Argo-CCI matchups (d). Only match-up pairs with

monthly CCI SSS are used to generate these maps.

Before co-locating TSG with CCI L4 SSS, a spatial smoothing is applied to TSG data to minimize the spatial representativeness uncertainty when comparing to the lower spatial resolution CCI L4 SSS product. The TSG data are spatially low-pass filtered using a running median filter with a window width of 25 km.

Each TSG smoothed data is then co-located with all CCI L4 SSS data found at grid nodes located within a radius of 12.5 km and +/-15 days (for the monthly CCI product) from the TSG data location. If several satellite SSS product samples are found to meet these criteria, the final satellite SSS match-up point is selected as the CCI L4 SSS whose central time is closest to the TSG measurement date.

4 Results

1. (a) Overview of large scale SSS variability

The ten-year long CCI L4 SSS time series witnesses large scale SSS anomalies, as shown by quarterly SSS anomalies (**Figure 7**). These SSS anomalies are particularly large in the tropical and subtropical bands and are detected with great realism as indicated by ISAS derived SSS anomalies (see supporting information S8). This comparison is fully independent as no information about interannual SSS variability coming from ISAS is introduced in the CCI+SSS OI. In areas strongy affected by rain, the comparison must be considered cautiously as the vertical representativeness of Argo and satellite SSS can contribute to non-negligible measurement differences. We shortly recall below the extreme events which occurred during this period and contributed to the main large-scale patterns of SSS variability. In the Pacific ocean, the 2010 and 2011 La Niña events generated strong anomalies in the western equatorial region (Hasson et al., 2014) followed by positive anomalies under the south Pacific convergence zone (SPCZ) in 2011 and 2012. The 2015-2016 extreme El Niño event first generated large negative anomalies in the equatorial region (Gasparin and Roemmich, 2016; Guimbard et al., 2017) which extend from the eastern Pacific fresh pool to the west of the basin, and which were further advected towards ~25°N (Hasson et al., 2018). In the tropical Indian Ocean, main large scale anomalies are associated with the Indian Ocean Dipole as first evidenced by (Durand et al., 2013). Also noticeable is the interannual variability of the large river plumes (Amazon, Congo, Niger…) where SMOS and SMAP have been shown to better detect variability associated with strong river discharges than in-situ gridded datasets (Fournier and Lee, 2021), providing a useful tool for a better understanding of interannual variability related to interactions between fresh plumes and ocean circulation (Akhil et al., 2020).

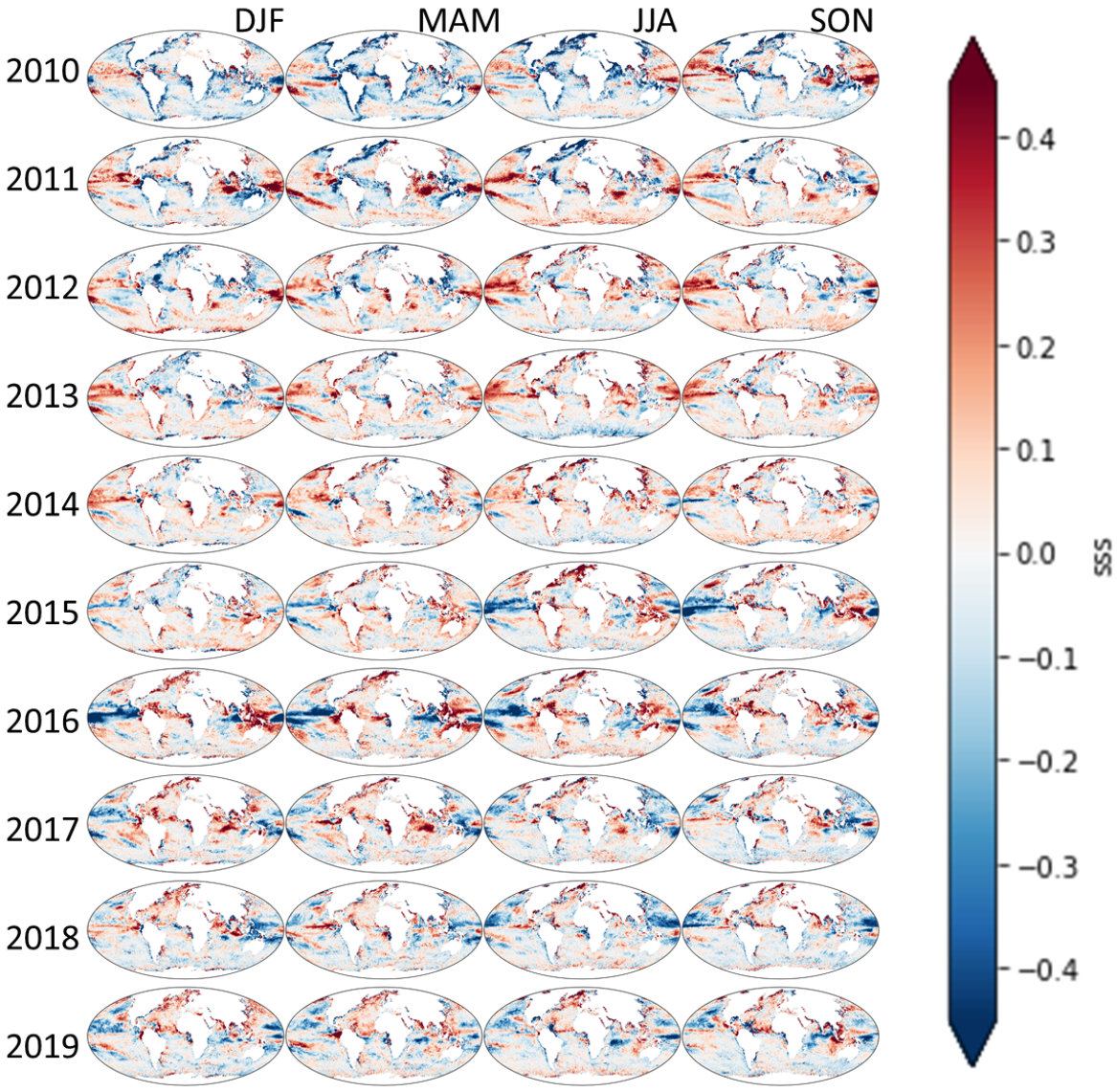

Figure 7: Quaterly SSS anomalies derived from L4 CCI SSS.

1. Comparisons with in-situ SSS:

The statistics of the comparisons between monthly CCI SSS and in-situ SSS are reported in **Table 4** to **Table 7**; the ones with weekly SSS are reported in the supporting information S9.

Over the global Ocean, when considering all matchups of monthly (weekly) CCI SSS with Argo SSS, the robust std difference is 0.16 (0.17), the std difference

is 0.27 (0.28), the determination coefficient, r^2, is 0.97 (0.97) (**Table 4**). When considering only match-up pairs acquired with no Rain Rate (RR) at in situ measurement time (RR=0 mm/h), the local 10 m height wind speed U10 is moderate, i.e., 3<U10 <12 m/s, the SST>5°C, and the distance to coast > 800 km (case C1 in PIMEP; **Table 5**), the robust std difference decreases to 0.13 (0.14), the std difference to 0.16 (0.17) and r^2 is 0.97(0.97). These metrics are amongst the best performance of satellite-Argo comparisons made at PIMEP (**Table 4** & **Table 5**).

Table 4: Statistics of monthly satellite SSS comparisons with Argo SSS (All matchups)

Statistics of ΔSSS (Satellite - Argo) - ALL

Satellite products	#	Median	Mean	Std	RMS	IQR	r^2	Std*
All period								
smos-l3-catds-locean-v5-18d	1269474	0.01	0.01	0.32	0.32	0.28	0.974	0.21
cci-l4-esa-merged-oi-v2.31-30dr	889299	0.00	0.00	0.27	0.27	0.21	0.969	0.16
SMOS+Aquarius period								
aquarius-l3-or-v5-1m	391630	-0.04	-0.09	0.47	0.48	0.28	0.899	0.21
aquarius-l3-jpl-v5-1m	368837	0.06	0.07	0.30	0.31	0.28	0.922	0.21
aquarius-l4-iprc-v5-1m	372010	0.00	-0.01	0.21	0.21	0.15	0.961	0.11
cci-l4-esa-merged-oi-v2.31-30dr	334414	0.01	0.01	0.28	0.28	0.21	0.961	0.16
SMOS+SMAP period								
smap-l3-rss-v4-1m	604522	-0.02	-0.05	0.39	0.40	0.27	0.980	0.20
smap-l3-jpl-v5.0-1m	614677	0.04	0.02	0.64	0.64	0.35	0.950	0.26
cci-l4-esa-merged-oi-v2.31-30dr	422977	-0.01	0.00	0.25	0.25	0.21	0.980	0.16

Table 5: Statistics of monthly satellite SSS comparisons with Argo SSS (only match-up pairs where RR=0 mm/h, 3<U10 <12 m/s, SST>5°C, distance to coast > 800 km)

Statistics of ΔSSS (Satellite - Argo) - C1

Satellite products	#	Median	Mean	Std	RMS	IQR	r^2	Std*
All period								
smos-l3-catds-locean-v5-18d	409987	0.01	0.01	0.19	0.20	0.23	0.958	0.17
cci-l4-esa-merged-oi-v2.31-30dr	301849	0.00	0.00	0.16	0.16	0.18	0.970	0.13
Aquarius period								
aquarius-l3-or-v5-1m	125302	-0.03	-0.03	0.19	0.19	0.21	0.961	0.16
aquarius-l3-jpl-v5-1m	122877	0.03	0.04	0.19	0.20	0.21	0.962	0.16
aquarius-l4-iprc-v5-1m	122889	0.00	0.00	0.13	0.13	0.13	0.981	0.10
cci-l4-esa-merged-oi-v2.31-30dr	111049	0.00	0.01	0.16	0.16	0.17	0.973	0.13
SMAP period								
smap-l3-rss-v4-1m	193751	-0.01	-0.02	0.18	0.18	0.20	0.964	0.15
smap-l3-jpl-v5.0-1m	197243	0.03	0.04	0.24	0.24	0.26	0.938	0.20
cci-l4-esa-merged-oi-v2.31-30dr	144537	-0.01	0.00	0.16	0.16	0.18	0.970	0.13

The large decrease in std difference between All cases and case C1 is in a large part due to the increasing sampling uncertainties between Argo and CCI fields in regions in the vicinity of land masses. With respect to the statistical indicators obtained with L3 SSS fields of each individual sensors, the std difference and the rms difference with CCI L4 SSS are systematically reduced, because of the noise reduction associated with the OI method. r^2 is much improved with respect to Aquarius L3, especially when considering "All cases". It is reduced when considering only open ocean data (0.95 with Aquarius weekly data instead of 0.97 with CCI weekly data) where variability at scales smaller than 100 km is significantly less than when the data are within a distance of 800 km from nearest coasts. The statistical comparisons with Argo exhibit better performances with Aquarius L4 data which are adjusted monthly with Argo SSS, contrary to CCI L4. Comparisons of CCI data with TSG (**Table 6** & **Table 7**) also show systematic improvement of all statistical indicators with respect to L3 SSS from individual sensors. The Aquarius L4 SSS still outscores CCI SSS in term of robust std difference but the std difference and r^2 for all cases comparisons are clearly better: the std difference of CCI SSS with respect to ship TSG SSS is 23% less and r^2 is higher by 16% for monthly CCI L4 SSS compared to Aquarius L4 SSS (**Table 6**). This is likely because ship TSGs dominantly explore tropical and mid-latitudes regions (**Figure 6**) and better sense SSS spatial variability than Argo punctual measurements, hence strengthening the better sampling of spatial SSS variability with CCI L4 SSS.

Table 6: Statistics of monthly satellite SSS comparisons with VOS Legos DM TSG and GOSUD RV TSG SSS (All matchups)

Statistics of ΔSSS (Satellite - TSG) - ALL								
Satellite products	**#**	**Median**	**Mean**	**Std**	**RMS**	**IQR**	**r^2**	**Std***
All period								
smos-l3-catds-locean-v5-18d	9705843	-0.01	0.02	0.64	0.64	0.40	0.882	0.30
cci-l4-esa-merged-oi-v2.31-30dr	5832430	-0.01	0.00	0.48	0.48	0.27	0.870	0.20
SMOS+Aquarius period								
aquarius-l3-or-v5-1m	2461314	-0.13	-0.29	1.22	1.25	0.53	0.484	0.36
aquarius-l3-jpl-v5-1m	2254751	0.07	0.12	0.87	0.88	0.39	0.590	0.29
aquarius-l4-iprc-v5-1m	2220427	0.00	0.08	0.71	0.72	0.22	0.726	0.17
cci-l4-esa-merged-oi-v2.31-30dr	1971061	-0.02	-0.01	0.55	0.55	0.30	0.845	0.22
SMOS+SMAP period								
smap-l3-rss-v4-1m	4817883	0.02	0.09	0.64	0.65	0.36	0.918	0.27
smap-l3-jpl-v5.0-1m	5094655	-0.01	0.00	0.85	0.85	0.40	0.869	0.30
cci-l4-esa-merged-oi-v2.31-30dr	2934792	0.00	0.02	0.41	0.41	0.23	0.901	0.17

Table 7: Statistics of monthly satellite SSS comparisons with VOS Legos DM TSG and GOSUD RV TSG SSS (only match-up pairs where RR=0 mm/h, 3<U10 <12 m/s, SST>5°C, distance to coast > 800 km)

Statistics of ΔSSS (Satellite - TSG) - C1								
Satellite products	**#**	**Median**	**Mean**	**Std**	**RMS**	**IQR**	**r^2**	**Std***
All period								
smos-l3-catds-locean-v5-18d	1074287	-0.01	0.00	0.20	0.20	0.24	0.959	0.18
cci-l4-esa-merged-oi-v2.31-30dr	798581	-0.01	-0.01	0.18	0.18	0.19	0.968	0.14
Aquarius period								
aquarius-l3-or-v5-1m	292990	-0.01	-0.01	0.22	0.22	0.24	0.958	0.18
aquarius-l3-jpl-v5-1m	286023	0.03	0.05	0.23	0.24	0.24	0.953	0.18
aquarius-l4-iprc-v5-1m	276580	-0.01	0.00	0.18	0.18	0.18	0.973	0.13
cci-l4-esa-merged-oi-v2.31-30dr	265588	-0.01	0.00	0.18	0.18	0.20	0.968	0.15
SMAP period								
smap-l3-rss-v4-1m	545538	-0.01	-0.02	0.18	0.18	0.20	0.969	0.15
smap-l3-jpl-v5.0-1m	560356	0.01	0.02	0.20	0.20	0.25	0.957	0.18
cci-l4-esa-merged-oi-v2.31-30dr	424268	0.00	0.00	0.17	0.17	0.18	0.970	0.14

To avoid the irregular spatial sampling of Argo matchups (Figure 6) while keeping significant number of matchups per grid point, the Argo/CCI pairwise MDB is re-gridded on the CCI grid subsampled by a factor of 7 both in latitude and longitude. It corresponds to an Equal Area EASE grid of resolution a 175 km. The same bi-weekly temporal sampling as CCI monthly product is conserved.

The median value for each grid point of all pairwise MDB values is taken. With this regular sampling, the CCI statistical indicators improve slightly: the robust std difference is 0.15, the std difference is 0.24. This is likely because of the Argo oversampling in regions strongly contaminated by RFIs (e.g., along Asian coasts; Figure 6).

The global pattern of the SSS, its variability and the global SSS statistical distribution are consistently observed by both Argo and the CCI+SSS fields (Figure 8). The spatial patterns are especially coherent in the tropics. At higher latitudes, the CCI+SSS variability in very dynamical regions (Gulf Stream, Agulhas current, Rio De La Plata river plume) appears slightly smaller with CCI fields than it is with Argo individual measurements, possibly due to variability at smaller spatio-temporal scale than 50 x 50 km^2 and one month. Contrarily, the CCI product variability is larger in regions with very low dynamics, e.g. in the Southern Ocean, likely a result of the increasing satellite SSS noise with decreasing temperatures.

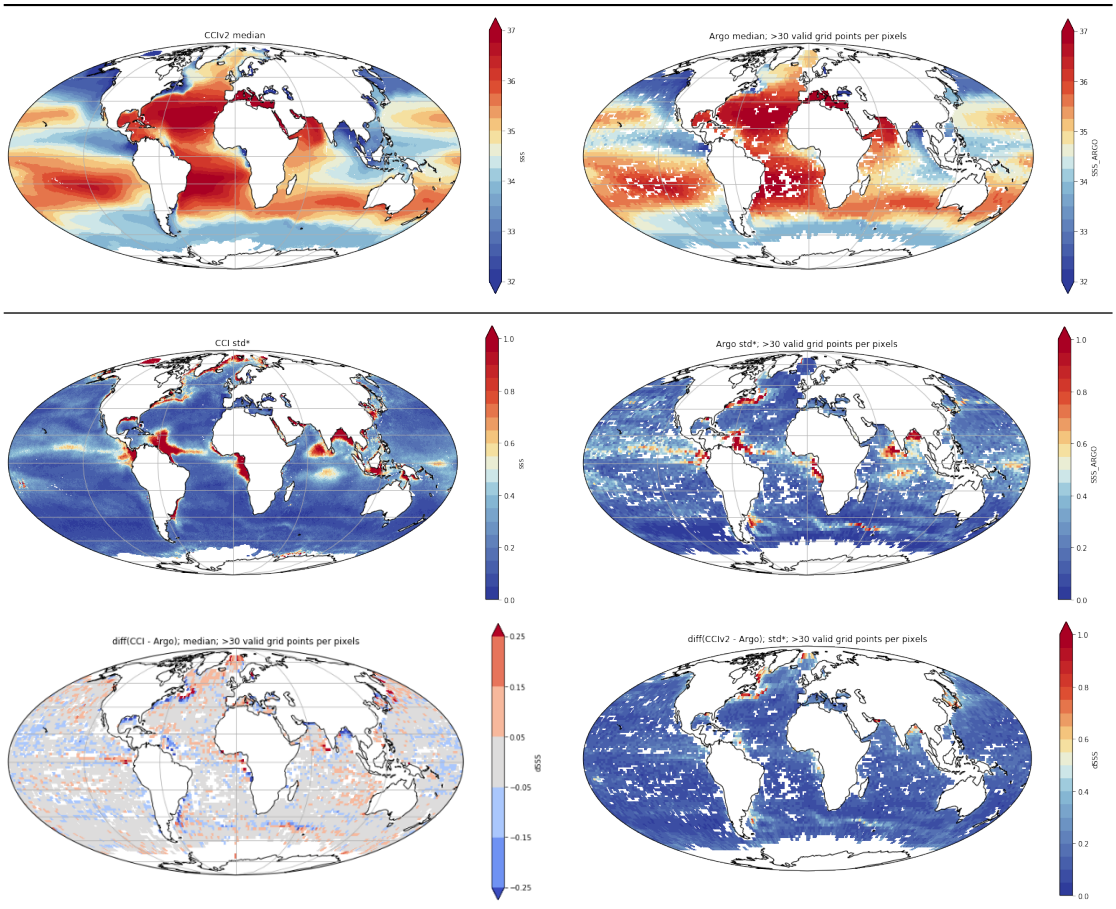

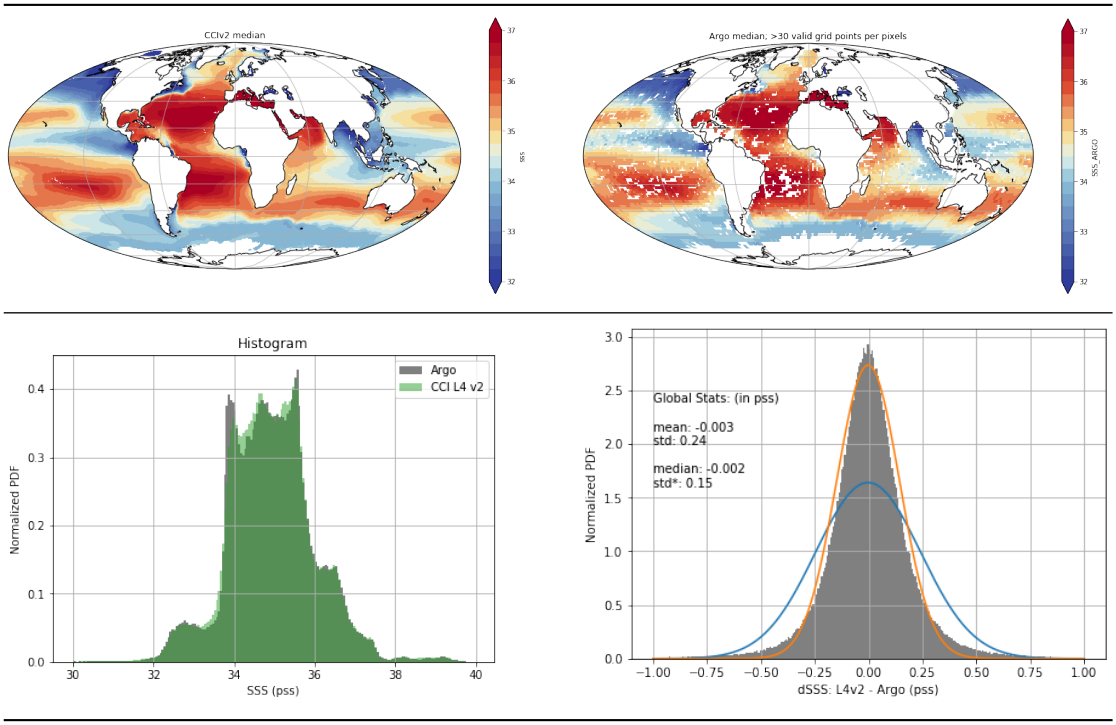

Figure 8: 1st row: median field computed on the full time series; (bottom) robust standard deviation. All four tops subfigures share the same color bar. 2nd row: (left) Temporal median and (right) temporal robust standard deviation of gridded pairwise SSS differences between CCI and Argo; 3rd row: (left) Temporal median and (right) temporal robust standard deviation of gridded pairwise SSS differences between CCI and Argo. 4th row: Histogram of all pairwise gridded data (left) Argo SSS in grey and CCI L4 v2 in green; (right) CCI L4 v2 minus Argo difference, (blue line) normal pdf using computed mean and std, (orange curve) normal pdf using computed median and robust std.

It is interesting to consider the temporal evolution of the median and std of the difference between CCI and Argo SSS (**Figure 9**). After mid-2011, the std difference decreases due to the inclusion of Aquarius SSS in the OI. Before mid-2015, the median difference varies seasonally (**Figure 9** and **Figure 10**): this due to both Aquarius and SMOS seasonal median differences (not shown). After mid-2015, the seasonal variations of the median differences are much reduced (**Figure 9** and **Figure 10**). This is possibly because the thermal model of the SMAP reflector was empirically adjusted using Argo temporal-latitudinal SSS profiles (Meissner et al., 2018). But we also noticed that seasonal latitudinal biases in SMOS SSS are reduced after 2015 (not shown). The largest differences are observed at high latitudes in cold waters where the sensitivity of radiometric L-band measurements to SSS is reduced and where the effect of the transitions

into and out of the sun eclipse is the largest (in boreal winter above 47°N for SMOS descending orbits).

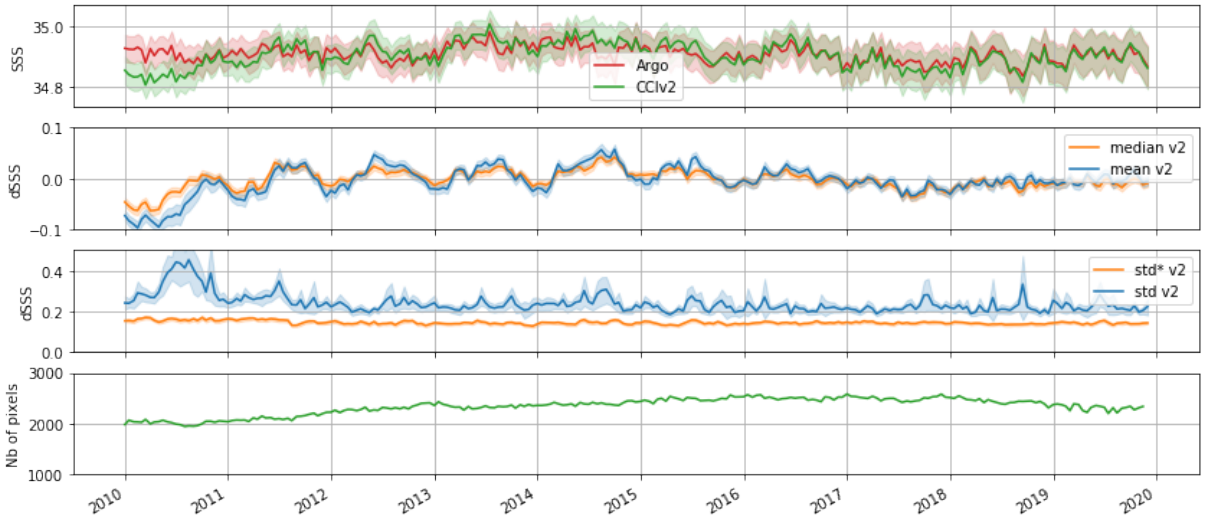

Figure 9: (1st panel): SSS mean of gridded pairwise Argo in red and L4 CCI SSS in black for v1 and green for v2; (2nd panel) Average of; (3rd panel) standard deviation of; the gridded pairwise SSS difference between CCI and Argo SSS. Blue and black dashed lines represent (2nd panel) the mean and (3rd panel) the standard deviation. Orange and solid black lines represent (2nd panel) the median and (3rd panel) the robust standard deviation. The shading indicates the 95% confidence interval.(4th panel): Number of gridded pairwise Argo and L4 CCI SSS.

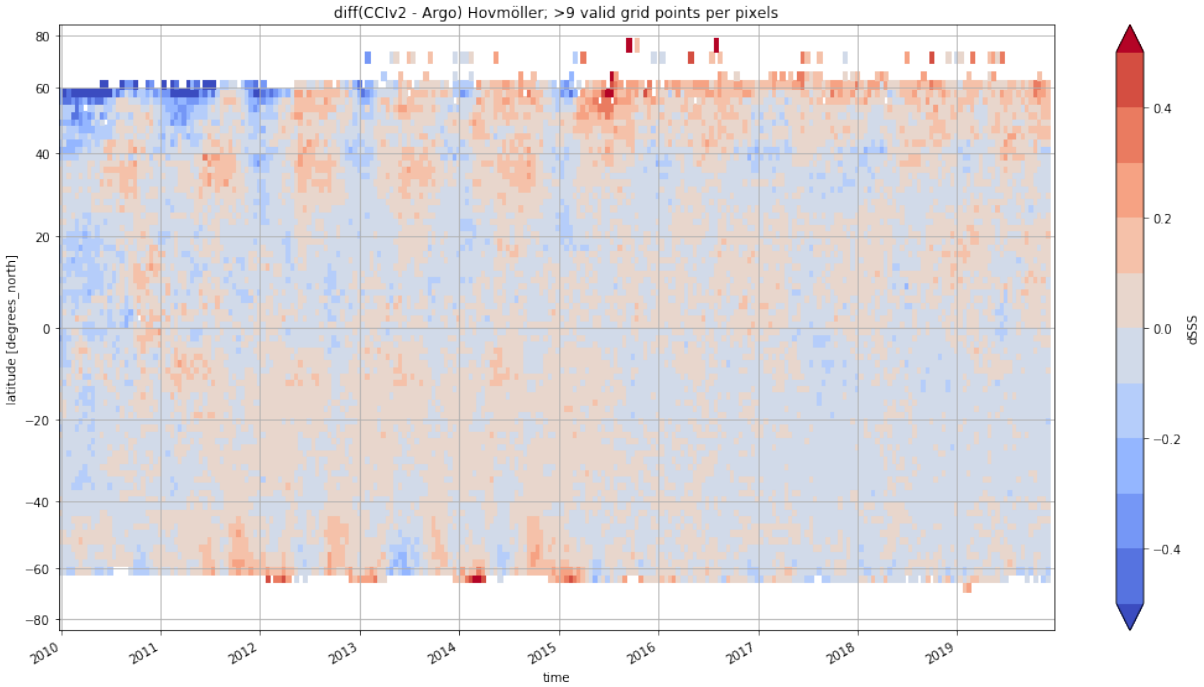

Figure 10: Global latitude-time Hovmöller of the gridded pairwise CCI difference with Argo

5 Discussion and Perspectives

For the first time, SSS measurements from the three L-band satellite sensors have been merged to produce CCI L4 SSS time series over a decade at global scale. No spatial smoothing nor temporal relaxation to in-situ SSS have been introduced in order to keep as much as possible SSS interannual variability sensed by original SSS satellite measurements. On another hand, the self-consistency between satellite SSS measured by the various sensors and under various geometries have been used to correct for systematic uncertainties. When compared with in-situ Argo SSS, the robust std of the difference over the global ocean is 0.15 with monthly CCI products, the coefficient of determination is 0.97. These performances outscore the ones obtained with fields built from individual satellite measurements, and the 50 x 50 km^2 spatial resolution of the CCI L4 SSS products provides one of the most realistic measure of SSS in very variable regions. The potential of the CCI L4 dataset for revealing new insights has been demonstrated already by various scientific studies. Focussing on the interannual variability of the SSS in the Bay of Bengal and on the signature of the river plumes, Akhil et al. (2020) found that CCI L4 SSS performed better than SSS retrieved from individual satellite sensors, thus confirming our results. In the tropical Atlantic Ocean, the CCI L4 SSS allowed to study large seasonal and interannual variability in the respective roles of salinity and temperature

on the development of the tropical instability waves (TIWs), and to show that, in the top 60-m of the ocean, salinity and temperature each contribute to about 50% of the TIWs perturbation potential energy (Olivier et al., 2020). CCI L4 SSS is also used to document events of freshwater transport from the shelf to the open ocean near Demarara rise in January-March since 2010, showing that such events occurred in 7 out of 10 years (Reverdin et al., 2021).

The specifications of the CCI fields have been defined in collaboration with their potential users. Their requirements are, for a large part, in line with the ones formulated by other user groups and/or in other contexts, e.g. summarized by the World Meteorological Organization (WMO) (https://www.wmo-sat.info/oscar/variables/view/sea_surface_salinity), by a former low frequency satellite user requirement study (Kerr et al. 2019) or by the Sub-seasonal to longer predictions (SSLP) group. What all these studies have in common is that accuracy requirements are between 0.1 to 0.3 (see https://www.wmo-sat.info/oscar/variables/view/sea_surface_salinity). While the spatial and temporal resolution requirements of the users and the previously mentioned studies are compatible with the Global Climate Observing System (GCOS) Implementation Plan (GCOS-200 (214) ; https://library.wmo.int/doc_num.php?explnum_id=3417), the GCOS uncertainty and stability requirements of 0.01 and 0.001 per decade respectively are an order of magnitude more stringent. These values, the same as the ones for subsurface in-situ data, appear very small compared to the SSS variability and to the spatio-temporal undersampling of this variability by in-situ near surface salinity measurements. Even with the increase of measurements associated with the full deployment of the Argo buoy network, in-situ near surface salinity measurements do not allow to reach such accuracy over all regions of the global ocean.

The methodology we have developed for building the CCI L4 dataset aims at preserving the SSS variability globally observed by satellite every few days in footprints integrated over typically 50 x 50 km^2. The bias corrections are mostly based on satellite measurements self-consistency criteria and are considering specific properties of each sensor measurements. External SSS information is considered only for calibrating the long term SSS absolute value and for estimating representativity uncertainties. The CCI+SSS approach is, therefore, upstream of the optimal interpolations which correct satellite SSS biases using in-situ SSS fields on a monthly basis or less, such as (Melnichenko et al., 2016), and the CCI+SSS fields could be used as inputs to such method, as was done with SMOS data (Nardelli et al., 2016) or with SMOS and SMAP data (Kolodziejczyk et al., 2020).

The improved accuracy of the CCI L4 SSS with respect to individual sensors SSS accuracy has been made possible because individual sensors SSS products were already shown to detect consistent variabilities. For instance, D'Addezio and Subrahmanyam (2016) showed that SMOS and Aquarius detect high SSS variability associated with the Agulhas current consistent with Argo SSS, whereas Fournier and Lee (2021) showed very consistent SMOS and SMAP SSS in river

plumes areas. Yu et al. (2021) and Bingham et al. (2021) found that SSS annual and semiannual amplitudes are quite well represented over the open ocean by the satellite SSS products considered for building the CCI L4 SSS.

Nevertheless, there is still room for improving CCI L4 SSS, their uncertainties and their validation. In particular, it would be interesting to reach a better stability of the CCI L4 SSS time series.

For instance, latitudinal differences remain with respect to Argo salinities, mostly before mid-2015. After mid-2015, both the inclusion of SMAP SSS and reduced SMOS SSS latitudinal biases are responsible for the improvement. The reason why SMOS SSS are more stable after mid-2015 is not entirely clear, even though a change in the SMOS calibration mode (warm Noise Injection Radiometer (NIR) calibration after November 2014) likely contributes to this improvement. An uncertainty on the temporal variability of SMOS SSS arises from the current use of an SSS climatology in the SMOS OTT region. The interannual variability of the median SSS over the OTT region, as determined from ISAS SSS, reaches +/-0.05 during the 2010-2019 period which could be corrected. The model for the dielectric constant of seawater at L-band in cold water has also been shown to remain an issue (Boutin et al., 2020). This will be corrected in the future CCI L4 SSS release. Another source of uncertainty comes from the varying versions of ECMWF forecast fields used as priors (wind speed, SST) in the SMOS SSS retrieval. The use of the same model version for the reanalyzed fields, such as reanalyses like ERA5, could help stabilize the time series. Last, an ongoing SMOS reprocessing with a revised calibration is more stable (preliminary results) and the level 1 revised algorithm corrects part of the sun contamination at the high northern latitudes. For Aquarius SSS, remaining systematic differences have been found between ascending and descending orbits (Kao et al., 2018; Meissner et al., 2018). We have not considered correcting Aquarius SSS for systematic latitudinal seasonal biases before merging with SMOS SSS, but this should be envisioned in the future. Future studies should also pay more attention to systematic differences arising from the components of the radiative transfer models and of the prior datasets which differ between the processing chains of each of the three sensors.

The development of version 2 of CCI L4 SSS first focused on low to mid latitudes regions where satellite SSS datasets were the most mature. Recent products (Supply et al., 2020b), (Olmedo et al., 2018), (Tang et al., 2018), (Brucker et al., 2014) are nevertheless achieving an accuracy useful for detecting Arctic Ocean freshwater changes (Fournier et al., 2020), changes in river plumes extent (Vazquez-Cuervo et al., 2021) and their relations to wind atmospheric forcing (Tarasenko et al., 2021). Hence keeping the best potentialities demonstrated with the existing datasets associated with the three satellite missions at high latitudes will be another remaining main challenge for the future research and developments of CCI+SSS merging algorithms.

In this CCI product version, no correction has been applied for rain effects on SMOS SSS products, because reliable rain estimates at hourly resolution as

provided by IMERG, and as required by correction or sorting methods (Supply et al., 2020a; Supply et al., 2018), were not available before 2014, i.e., at the time of the CCI+SSS version 2 development. Nevertheless, this effect might be non-negligible, even on monthly SSS estimates in the rainiest regions of the globe. In very rainy regions such as the Pacific ITCZ, (Boutin et al., 2014) (their Figure 9) estimated that vertical representativeness mismatch might lead to differences between monthly salinity at a few meters depth and in the first centimeter depth of up to 0.5 at satellite pixel level (50x50 km^2). Nevertheless, this effect is very patchy, and when averaged over all longitudes, it is mostly less than 0.1, except in very abnormal conditions such as in the second part of 2015, when it reached up to 0.15 in the latitudinal band affected by the freshest anomalies (Supply et al. PhD thesis 2020). During this 2015 abnormal period, modelled salinities at 10 m depth and satellite SSS in the northern tropical Pacific Ocean also differed by this order of magnitude (Hasson et al., 2018). Thus, even though this effect did not hamper the detection of 2015 large scale SSS anomalies, and that an estimate of the freshening at 1 cm depth could also be of interest for air-sea interactions studies, it will be important in future CCI L4 SSS releases to provide an estimate of CCI L4 SSS corrected from the vertical representativeness effect.

Validation with standard statistical indicators such as the ones used in this paper has inherent limitations. For instance, high-resolution fields might appear as having a higher rms difference with respect to reference fields than lower resolution fields when representativeness errors between reference fields and high-resolution fields are important. This effect contributes to some lower rms difference observed with Aquarius than with CCI L4 SSS. We identified it by looking at r^2, but methodologies such as the ones developed in high resolution modelling community (Crocker et al., 2020) could be investigated to better quantify the accuracy of high-resolution fields relative to lower resolution fields. Wavenumber spectra analysis, such as the one performed on sea surface height by (Dufau et al., 2016), should also be studied in order to validate dynamical features of SSS at various spatio-temporal scales.

The characterization of SSS variability remains challenging as, on one hand, the combination of in-situ and satellite information remains to be improved (Stammer et al., 2021); and on the other hand, regions with high SSS variability such as the river plumes or strong surface currents regions are the ones benefiting the most from the satellite information (Tranchant et al., 2019). The statistical distribution of SSS is not expected to be Gaussian (Bingham et al., 2002), especially in regions affected by fresh water inputs, so that vertical, temporal and spatial representativeness errors between in-situ and satellite measurements are not expected to be Gaussian. In particular, the SSS distributions are expected to be skewed towards low SSS values while the higher part of the SSS distributions are expected to vary much less. This lead us to adopt an adjustment of the full time series of CCI L4 SSS and ISAS SSS in fresh and very variable regions based on a high quantile of their statistical distributions. Nevertheless, OI assumption of Gaussian errors might lead to some drawbacks in fresh regions

such as river plumes or rainy areas, e.g., an artificial increase (decrease) of the uncertainty during periods with decreased (increased) variability that are very difficult to quantify given the sparseness of existing in-situ measurements. For the reasons outlined above, the validation of the SSS and its uncertainty estimate is very tricky and require extended research to go beyond the relatively crude validation presented in this paper.

Finally, in future versions of the CCI products, we plan to develop several regional products with longer time series than the one presented in this paper by extending the L-band based SSS back in time to 2002 over four large and warm river plume regions (1) Mississippi; (2) Orinoco and Amazon; (3) Niger and Congo and (4) Bay of Bengal. For this, we will complement the observations provided by the suite of L-band sensors using AMSR-E lowest microwave frequency channel data (at 6.9 GHz=C-band and 10.7 GHz=X-band) acquired in warm and strongly contrasted dynamical river plume regions. In such conditions, the small SSS signal contained in C-band radiometer data is improved by differentiating the vertical polarization surface reflectance between the C and X band, minimizing SST and wind effects on the data. Monthly-averaged SSS retrievals using such approaches have been already demonstrated from AMSR-E data for the Amazon plume region (Reul et al., 2009) and from HY2-A data for the freshwater runoff near the Yangtze Delta (Song and Wang, 2017). In the future, new missions such as the Copernicus Imaging Microwave Radiometer (Donlon, 2020) and the SMOS-High Resolution mission (Rodríguez-Fernández et al., 2019) will benefit from the methods and approaches pioneered by the SSS-CCI activities and extend the climate record of satellite SSS into the 2040's.

Acknowledgments, Samples, and Data

We thank F. Bonjean for careful remarks about this manuscript, X. Perrot and J. Vialard for their feedbacks about the dataset and very fruitful discussions. SSS CCI datasets are freely available at https://catalogue.ceda.ac.uk/uuid/4ce685bff631459fb2a30faa699f3fc5. The PIMEP MDB are freely available as NetCDF files at ftp://ftp.ifremer.fr/ifremer/cersat/pimep/diffusion/data/; corresponding validation reports are available on https://pimep.ifremer.fr/diffusion/data/. SMAP salinity data are produced by Remote Sensing Systems and sponsored by the NASA Ocean Salinity Science Team. Data are available at www.remss.com. Aquarius data are available at https://podaac.jpl.nasa.gov/dataset/AQUARIUS_L3_SSS_SMID_ANNUAL_V5. CATDS SSS are available at the CATDS Production Data Center (CPDC), www.catds.fr. ISAS fields are taken from https://catalogue.marine.copernicus.eu/ (INSITU_GLO_TS_OA_REP_OBSERVATIONS_013_002 product). The GOSUD RV dataset is available at https://doi.org/10.17882/39475, the ships of opportunity dataset is available at http://www.legos.obs-mip.fr/observations/sss/datadelivery/dmdata. Argo data are taken from http://www.coriolis.eu.org/. This study was funded by ESA CCI contract 4000123663/18/I-NB.

References

https://doi.org/10.1016/j.rse.2020.111964

https://doi.org/10.1016/j.dsr.2015.08.005

https://doi.org/10.1029/2011JC007372

https://smos.argans.co.uk/docs/technotes/SO-RP-ARG-GS-0100_L2OS_Reprocessing_Report_v2.0_160229.

https://doi.org/10.1029/2000JC000767

https://doi.org/10.1002/2014JC010070

https://doi.org/10.1016/j.rse.2018.05.022

https://doi.org/10.1016/0011-7471(76)90001-2

https://doi.org/10.12770/12777edd12308-14296-14774-b12776f12773-12775b38
301cee12718

http://tpos2020.org/first-report/

https://doi.org/10.1016/j.rse.2016.02.006

https://doi.org/10.1016/j.dsr.2004.11.012

https://esamultimedia.esa.int/docs/EarthObservation/CIMR-MRD-v4.0-
20201006_Issued.pdf

https://doi.org/10.1002/2015JC010904

https://doi.org/10.1002/2016GL071712

https://doi.org/10.1016/j.rse.2016.02.050

https://doi.org/10.1029/2020JC016110

https://doi.org/10.1002/2016GL069542

https://doi.org/10.1002/2016JC012130

https://doi.org/10.1002/2013JC009388

https://doi.org/10.1029/2018JC014175

https://doi.org/10.1002/2017JC013423

https://doi.org/10.1029/2020GL088252

https://doi.org/10.1029/2020JC017041

https://doi.org/10.1029/2020GL091277

https://mycore.core-cloud.net/index.php/s/Y3tpySnNhI9HWUH

https://doi.org/10.1016/j.rse.2016.02.061

https://doi.org/10.1002/2013JC009248

https://doi.org/10.3390/rs11242989

www.remss.com/missions/smap

https://doi.org/10.1002/2015JC011343

https://doi.org/10.1016/j.rse.2015.12.052

https://doi.org/10.1016/j.rse.2016.01.013

https://doi.org/10.1029/2020JC016641

https://doi.org/10.1029/2020GL091478

https://doi.org/10.1002/2014GL059215

https://doi.org/10.1016/j.rse.2020.111769

https://doi.org/10.1029/2009GL038860

https://doi.org/10.1029/2007JC004623

https://doi.org/10.1029/2000JC000679

https://doi.org/10.1016/j.pocean.2020.102478

https://doi.org/10.1016/j.rse.2020.112027

https://doi.org/10.1002/qj.3110

https://doi.org/10.1029/2020JC016789

Akhil, V. P., J. Vialard, M. Lengaigne, M. G. Keerthi, J. Boutin, J. L. Vergely, and F. Papa (2020), Bay of Bengal Sea surface salinity variability using a decade of improved SMOS re-processing, *Remote Sensing of Environment*, *248*, 111964, doi:.Alory, G., et al. (2015), The French contribution to the voluntary observing ships network of sea surface salinity, *Deep Sea Research Part I: Oceanographic Research Papers*, *105*, 1-18, doi:.Anguelova, M. D., and P. W. Gaiser (2011), Skin depth at microwave frequencies of sea foam layers with vertical profile of void fraction, *Journal of Geophysical Research: Oceans*, *116*(C11), doi:.ARGO (2020), Argo float data and metadata from Global Data Assembly Centre (Argo GDAC), *SEANOE*, doi:10.17882/42182.Arias, M., and SMOS_Ocean_Expert_Support_Laboratories (2016), L2OS v622 Reprocessing Report, *Rep. SO-RP-ARG-GS-0100 Issue:2, available on* .Balaguru, K., G. R. Foltz, L. R. Leung, J. Kaplan, W. Xu, N. Reul, and B. Chapron (2020), Pronounced Impact of Salinity on Rapidly Intensifying Tropical Cyclones, *Bulletin of the American Meteorological Society*, *101*(9), E1497-E1511, doi:10.1175/bams-d-19-0303.1.Bindoff, N. L., W. W. L. Cheung, and J. A. J.G. Kairo, V.A. Guinder, R.Hallberg, N.Hilmi, N.Jiao, M.S. Karim, L.Levin,S. O'Donoghue, S.R. Purca Cuicapusa, B.Rinkevich,T.Suga, A.Tagliabue, and P.Williamson (2019), Changing Ocean, Marine Ecosystems, and Dependent Communities. In: IPCC Special Report on the Ocean and Cryosphere in a Changing Climate [H.-O. Pörtner, D.C. Roberts, V. Masson-Delmotte, P. Zhai, M. Tignor, E. Poloczanska, K. Mintenbeck, A. Alegría, M. Nicolai, A. Okem, J. Petzold, B. Rama, N.M. Weyer (eds.)]. In press.*Rep.*Bingham, F. M., S.

Brodnitz, and L. Yu (2021), Sea Surface Salinity Seasonal Variability in the Tropics from Satellites, Gridded In Situ Products and Mooring Observations, *Remote Sensing*, *13*(1), 110.Bingham, F. M., S. D. Howden, and C. J. Koblinsky (2002), Sea surface salinity measurements in the historical database, *Journal of Geophysical Research: Oceans*, *107*(C12), SRF 20-21-SRF 20-10, doi:.Boutin, J., N. Martin, G. Reverdin, S. Morisset, X. Yin, L. Centurioni, and N. Reul (2014), Sea surface salinity under rain cells: SMOS satellite and in situ drifters observations, *Journal of Geophysical Research: Oceans*, *119*(8), 5533-5545, doi:.Boutin, J., J.-L. Vergely, E. P. Dinnat, P. Waldteufel, F. D'Amico, N. Reul, A. Supply, and C. Thouvenin-Masson (2020), Correcting Sea Surface Temperature Spurious Effects in Salinity Retrieved From Spaceborne L-Band Radiometer Measurements, *IEEE Transactions on Geoscience and Remote Sensing*, 1-14, doi:10.1109/tgrs.2020.3030488.Boutin, J., J. L. Vergely, S. Marchand, F. D'Amico, A. Hasson, N. Kolodziejczyk, N. Reul, G. Reverdin, and J. Vialard (2018), New SMOS Sea Surface Salinity with reduced systematic errors and improved variability, *Remote Sensing of Environment*, *214*, 115-134, doi:.Bretherton, F. P., R. E. Davis, and C. B. Fandry (1976), A technique for objective analysis and design of oceanographic experiments applied to MODE-73, *Deep Sea Research and Oceanographic Abstracts*, *23*(7), 559-582, doi:.Brodzik, M. J., B. Billingsley, T. Haran, B. Raup, and M. H. Savoie (2012), EASE-Grid 2.0: Incremental but Significant Improvements for Earth-Gridded Data Sets, *ISPRS International Journal of Geo-Information*, *1*(1), 32-45.Brown, C. W., J. Boutin, and L. Merlivat (2015), New insights into fCO_2 variability in the tropical eastern Pacific Ocean using SMOS SSS, *Biogeosciences*, *12*(23), 7315-7329, doi:10.5194/bg-12-7315-2015.Brucker, L., E. P. Dinnat, and L. S. Koenig (2014), Weekly gridded Aquarius L-band radiometer/scatterometer observations and salinity retrievals over the polar regions – Part 2: Initial product analysis, *The Cryosphere*, *8*(3), 915-930, doi:10.5194/tc-8-915-2014.Carmack, E. C., et al. (2016), Freshwater and its role in the Arctic Marine System: Sources, disposition, storage, export, and physical and biogeochemical consequences in the Arctic and global oceans, *J Geophys Res-Biogeo*, *121*(3), 675-717, doi:10.1002/2015jg003140.CATDS (2017), CATDS-PDC L3OS 2P - Daily valid ocean salinity values product from SMOS satellite, edited, pp. .Cravatte, S., W. S . Kessler, N. Smith, S. E. Wijffels, and Contributing Authors (2016), First Report of TPOS 2020. GOOS-215, 200 pp. [Available online at .] *Rep.*Crocker, R., J. Maksymczuk, M. Mittermaier, M. Tonani, and C. Pequignet (2020), An approach to the verification of high-resolution ocean models using spatial methods, *Ocean Sci.*, *16*(4), 831-845, doi:10.5194/os-16-831-2020.D'Addezio, J. M., and B. Subrahmanyam (2016), Sea surface salinity variability in the Agulhas Current region inferred from SMOS and Aquarius, *Remote Sensing of Environment*, *180*, 440-452, doi:.Delcroix, T., M. J. McPhaden, A. Dessier, and Y. Gouriou (2005), Time and space scales for sea surface salinity in the tropical oceans, *Deep Sea Research Part I: Oceanographic Research Papers*, *52*(5), 787-813, doi:.Dinnat, E. P., D. M. Le Vine, J. Boutin, T. Meissner, and G. Lagerloef (2019), Remote Sensing of Sea Surface Salinity: Comparison of Satellite and In

Situ Observations and Impact of Retrieval Parameters, *Remote Sensing*, *11*(7), 750.Donlon, C. J. (2020), The Copernicus Imaging Microwave Radiometer (CIMR) Mission Requirements Document, v4.0, available from .Drushka, K., W. E. Asher, A. T. Jessup, E. J. Thompson, S. Lyer, and D. Clark (2019), Capturing Fresh Layers with the Surface Salinity Profiler, *Oceanography*, *32*.Dufau, C., M. Orsztynowicz, G. Dibarboure, R. Morrow, and P.-Y. Le Traon (2016), Mesoscale resolution capability of altimetry: Present and future, *Journal of Geophysical Research: Oceans*, *121*(7), 4910-4927, doi:.Durack, P. J., S. E. Wijffels, and R. J. Matear (2012), Ocean salinities reveal strong global water cycle intensification during 1950 to 2000, *Science*, *336*(6080), 455-458, doi:10.1126/science.1212222.Durand, F., G. Alory, R. Dussin, and N. Reul (2013), SMOS reveals the signature of Indian Ocean Dipole events, *Ocean Dynamics*, *63*(11), 1203-1212, doi:10.1007/s10236-013-0660-y.Fine, R. A., D. A. Willey, and F. J. Millero (2017), Global variability and changes in ocean total alkalinity from Aquarius satellite data, *Geophysical Research Letters*, *44*(1), 261-267, doi:.Foltz, G. R., et al. (2019), The Tropical Atlantic Observing System, *Frontiers in Marine Science*, *6*(206), doi:10.3389/fmars.2019.00206.Font, J., A. Camps, A. Borges, M. Martín-Neira, J. Boutin, N. Reul, Y. H. Kerr, A. Hahne, and S. Mecklenburg (2010), SMOS: The Challenging Sea Surface Salinity Measurement From Space, *Proceedings of the IEEE*, *98*(5), 649-665.Fournier, S., and T. Lee (2021), Seasonal and Interannual Variability of Sea Surface Salinity Near Major River Mouths of the World Ocean Inferred from Gridded Satellite and In-Situ Salinity Products, *Remote Sensing*, *13*(4), 728.Fournier, S., T. Lee, and M. M. Gierach (2016), Seasonal and interannual variations of sea surface salinity associated with the Mississippi River plume observed by SMOS and Aquarius, *Remote Sensing of Environment*, *180*, 431-439, doi:.Fournier, S., T. Lee, X. Wang, T. W. K. Armitage, O. Wang, I. Fukumori, and R. Kwok (2020), Sea Surface Salinity as a Proxy for Arctic Ocean Freshwater Changes, *Journal of Geophysical Research: Oceans*, *125*(7), e2020JC016110, doi:.Gaillard, F., T. Reynaud, V. Thierry, N. Kolodziejczyk, and K. v. Schuckmann (2016), In Situ–Based Reanalysis of the Global Ocean Temperature and Salinity with ISAS: Variability of the Heat Content and Steric Height, *Journal of Climate*, *29*(4), 1305-1323, doi:10.1175/jcli-d-15-0028.1.Gasparin, F., and D. Roemmich (2016), The strong freshwater anomaly during the onset of the 2015/2016 El Niño, *Geophysical Research Letters*, *43*(12), 6452-6460, doi:.Guimbard, S., N. Reul, B. Chapron, M. Umbert, and C. Maes (2017), Seasonal and interannual variability of the Eastern Tropical Pacific Fresh Pool, *Journal of Geophysical Research: Oceans*, *122*(3), 1749-1771, doi:.Hackert, E., R. M. Kovach, A. Molod, G. Vernieres, A. Borovikov, J. Marshak, and Y. Chang (2020), Satellite Sea Surface Salinity Observations Impact on El Niño/Southern Oscillation Predictions: Case Studies From the NASA GEOS Seasonal Forecast System, *Journal of Geophysical Research: Oceans*, *125*(4), e2019JC015788, doi:10.1029/2019jc015788.Hasson, A., T. Delcroix, J. Boutin, R. Dussin, and J. Ballabrera-Poy (2014), Analyzing the 2010–2011 La Niña signature in the tropical Pacific sea surface salinity using in situ data, SMOS observations, and a numerical simulation, *Journal of Geophysical Research:*

Oceans, *119*(6), 3855-3867, doi:.Hasson, A., J. T. Farrar, J. Boutin, F. Bingham, and T. Lee (2019), Intraseasonal Variability of Surface Salinity in the Eastern Tropical Pacific Associated With Mesoscale Eddies, *Journal of Geophysical Research: Oceans*, *124*(4), 2861-2875, doi:.Hasson, A., M. Puy, J. Boutin, E. Guilyardi, and R. Morrow (2018), Northward Pathway Across the Tropical North Pacific Ocean Revealed by Surface Salinity: How do El Niño Anomalies Reach Hawaii?, *Journal of Geophysical Research: Oceans*, *123*(4), 2697-2715, doi:.Ho, D. T., and J. J. Schanze (2020), Precipitation-Induced Reduction in Surface Ocean pCO2: Observations From the Eastern Tropical Pacific Ocean, *Geophysical Research Letters*, *47*(15), e2020GL088252, doi:.Houndegnonto, O. J., N. Kolodziejczyk, C. Maes, B. Bourlès, C. Y. Da-Allada, and N. Reul (2021), Seasonal Variability of Freshwater Plumes in the Eastern Gulf of Guinea as Inferred From Satellite Measurements, *Journal of Geophysical Research: Oceans*, *126*(5), e2020JC017041, doi:.Huang, M., X. Liang, Y. Zhu, Y. Liu, and R. H. Weisberg (2021), Eddies Connect the Tropical Atlantic Ocean and the Gulf of Mexico, *Geophysical Research Letters*, *48*(4), e2020GL091277, doi:.Ibánhez, J. S. P., M. Flores, and N. Lefèvre (2017), Collapse of the tropical and subtropical North Atlantic CO2 sink in boreal spring of 2010, *Scientific Reports*, *7*(1), 41694, doi:10.1038/srep41694.Kao, H.-Y., G. S. E. Lagerloef, T. Lee, O. Melnichenko, T. Meissner, and P. Hacker (2018), Assessment of Aquarius Sea Surface Salinity, *Remote Sens.*, *10(9):1341*.Kerr, Y., et al. (2019), Low Frequency Passive Microwave User Requirement Consolidation Study, Issue 2,*Rep. SO-TN-CB-GS-0075*, CESBIO, Toulouse, .Kerr, Y., et al. (2010), The SMOS Mission: New Tool for Monitoring Key Elements ofthe Global Water Cycle, *Proceedings of the IEEE*, *98*(5), 666-687.Klein, L., and C. Swift (1977), An improved model for the dielectric constant of sea water at microwave frequencies, *IEEE Transactions on Antennas and Propagation*, *25*(1), 104-111.Kolodziejczyk, N., J. Boutin, J.-L. Vergely, S. Marchand, N. Martin, and G. Reverdin (2016), Mitigation of systematic errors in SMOS sea surface salinity, *Remote Sensing of Environment*, *180*, 164-177, doi:.Kolodziejczyk, N., D. Diverres, S. Jacquin, Y. Gouriou, J. Grelet, M. Le Menn, J. Tassel, G. Reverdin, C. Maes, and F. Gaillard (2020), Sea Surface Salinity from French RESearcH Vessels : Delayed mode dataset, annual release, edited, SEANOE, doi:10.17882/39475.Kolodziejczyk, N., M. Hamon, J. Boutin, J.-L. Vergely, G. Reverdin, A. Supply, and N. Reul (2021), Objective Analysis of SMOS and SMAP Sea Surface Salinity to Reduce Large-Scale and Time-Dependent Biases from Low to High Latitudes, *Journal of Atmospheric and Oceanic Technology*, *38*(3), 405-421, doi:10.1175/jtech-d-20-0093.1.Kristensen, S. S., N. Skou, S. S. Søbjærg, and J. E. Balling (2019), Developments of RFI Detection Algorithms and Their Application to Future European Spaceborne Systems, paper presented at IGARSS 2019 - 2019 IEEE International Geoscience and Remote Sensing Symposium, 28 July-2 Aug. 2019.Lagerloef, G., et al. (2008), The Aquarius/SAC-D Mission: Designed to Meet the Salinity Remote-Sensing Challenge, *Oceanography*, *21*.Land, P. E., et al. (2015), Salinity from Space Unlocks Satellite-Based Assessment of Ocean Acidification, *Environ Sci Technol*, *49*(4), 1987-1994, doi:10.1021/es504849s.Le Vine, D. M., and P. d.

Matthaeis (2014), Aquarius Active/Passive RFI Environment at L-Band, *IEEE Geoscience and Remote Sensing Letters*, *11*(10), 1747-1751.Lefèvre, N., D. F. Urbano, F. Gallois, and D. Diverrès (2014), Impact of physical processes on the seasonal distribution of the fugacity of CO2 in the western tropical Atlantic, *Journal of Geophysical Research: Oceans*, *119*(2), 646-663, doi:.Li, L., R. W. Schmitt, C. C. Ummenhofer, and K. B. Karnauskas (2016), North Atlantic salinity as a predictor of Sahel rainfall, *Sci Adv*, *2*(5), e1501588, doi:10.1126/sciadv.1501588.Lin, X. Q., Y.; Sun, D. (2019), Thermohaline Structures and Heat/Freshwater Transports of Mesoscale Eddies in the Bay of Bengal Observed by Argo and Satellite Data, *Remote Sens.*, *11, 2989*, doi:.Lique, C. (2015), Arctic sea ice heated from below, *Nat Geosci*, *8*(3), 172-173, doi:10.1038/ngeo2357.Lukas, R., and E. Lindstrom (1991), The Mixed Layer of the Western Equatorial Pacific-Ocean, *J Geophys Res-Oceans*, *96*, 3343-3357, doi:Doi 10.1029/90jc01951.Meissner, T., F. J. Wentz, and D. M. Le Vine (2018), The Salinity Retrieval Algorithms for the NASA Aquarius Version 5 and SMAP Version 3 Releases, *Remote Sensing*, *10*(7), 1121.Meissner, T., F. J. Wentz, A. Manaster, and R. Lindsley (2019), Remote Sensing Systems SMAP Ocean Surface Salinities [Level 2C], Version 4.0 validated release edited by S. R. Remote Sensing Systems, CA, USA. Available online at , doi:10.5067/SMP40-2SOCS Melnichenko, O., P. Hacker, N. Maximenko, G. Lagerloef, and J. Potemra (2016), Optimum interpolation analysis of Aquarius sea surface salinity, *Journal of Geophysical Research: Oceans*, *121*(1), 602-616, doi:.Melnichenko, O., P. Hacker, and V. Müller (2021), Observations of Mesoscale Eddies in Satellite SSS and Inferred Eddy Salt Transport, *Remote Sensing*, *13*(2), 315.Millero, F. J. (2007), The Marine Inorganic Carbon Cycle, *Chemical Reviews*, *107*(2), 308-341, doi:10.1021/cr0503557.Nardelli, B., R. Droghei, and R. Santoleri (2016), Multi-dimensional interpolation of SMOS sea surface salinity with surface temperature and in situ salinity data, *Remote Sensing of Environment*, *180*, 392-402, doi:.Oliva, R., et al. (2016), Status of Radio Frequency Interference (RFI) in the 1400–1427MHz passive band based on six years of SMOS mission, *Remote Sensing of Environment*, *180*, 64-75, doi:.Olivier, L., G. Reverdin, A. Hasson, and J. Boutin (2020), Tropical Instability Waves in the Atlantic Ocean: Investigating the Relative Role of Sea Surface Salinity and Temperature From 2010 to 2018, *Journal of Geophysical Research: Oceans*, *125*(12), e2020JC016641, doi:.Olmedo, E., C. Gabarró, V. González-Gambau, J. Martínez, J. Ballabrera-Poy, A. Turiel, M. Portabella, S. Fournier, and T. Lee (2018), Seven Years of SMOS Sea Surface Salinity at High Latitudes: Variability in Arctic and Sub-Arctic Regions, *Remote Sensing*, *10*(11), 1772.Picaut, J., M. Ioualalen, T. Delcroix, F. Masia, R. Murtugudde, and J. Vialard (2001), The oceanic zone of convergence on the eastern edge of the Pacific warm pool: A synthesis of results and implications for El Nino-Southern Oscillation and biogeochemical phenomena, *J Geophys Res-Oceans*, *106*(C2), 2363-2386, doi:Doi 10.1029/2000jc900141.Piepmeier, J. R., et al. (2017), SMAP L-Band Microwave Radiometer: Instrument Design and First Year on Orbit, *IEEE Transactions on Geoscience and Remote Sensing*, *55*(4), 1954-1966.Qu, T. D., and J. Y. Yu (2014), ENSO

indices from sea surface salinity observed by Aquarius and Argo, *J Oceanogr*, *70*(4), 367-375, doi:10.1007/s10872-014-0238-4.Reul, N., B. Chapron, S. A. Grodsky, S. Guimbard, V. Kudryavtsev, G. R. Foltz, and K. Balaguru (2021), Satellite Observations of the Sea Surface Salinity Response to Tropical Cyclones, *Geophysical Research Letters*, *48*(1), e2020GL091478, doi:.Reul, N., B. Chapron, T. Lee, C. Donlon, J. Boutin, and G. Alory (2014), Sea surface salinity structure of the meandering Gulf Stream revealed by SMOS sensor, *Geophysical Research Letters*, *41*(9), 3141-3148, doi:.Reul, N., et al. (2020), Sea surface salinity estimates from spaceborne L-band radiometers: An overview of the first decade of observation (2010–2019), *Remote Sensing of Environment*, *242*, 111769, doi:.Reul, N., S. Saux-Picart, B. Chapron, D. Vandemark, J. Tournadre, and J. Salisbury (2009), Demonstration of ocean surface salinity microwave measurements from space using AMSR-E data over the Amazon plume, *Geophysical Research Letters*, *36*(13), doi:.Reverdin, G., et al. (2021), Formation and Evolution of a Freshwater Plume in the Northwestern Tropical Atlantic in February 2020, *Journal of Geophysical Research: Oceans*, *126*(4), e2020JC016981, doi:10.1029/2020jc016981.Rodríguez-Fernández, N. J., et al. (2019), SMOS-HR: A High Resolution L-Band Passive Radiometer for Earth Science and Applications, paper presented at IGARSS 2019 - 2019 IEEE International Geoscience and Remote Sensing Symposium, 28 July-2 Aug. 2019.Roemmich, D., et al. (2019), On the Future of Argo: A Global, Full-Depth, Multi-Disciplinary Array, *Frontiers in Marine Science*, *6*, doi:ARTN 43910.3389/fmars.2019.00439.Salisbury, J., et al. (2015), How Can Present and Future Satellite Missions Support Scientific Studies that Address Ocean Acidification?, *Oceanography*, *28*.Sengupta, D., S. R. Parampil, G. S. Bhat, V. S. N. Murty, V. Ramesh Babu, T. Sudhakar, K. Premkumar, and Y. Pradhan (2008), Warm pool thermodynamics from the Arabian Sea Monsoon Experiment (ARMEX), *Journal of Geophysical Research: Oceans*, *113*(C10), doi:.Shenoi, S. S. C., D. Shankar, and S. R. Shetye (2002), Differences in heat budgets of the near-surface Arabian Sea and Bay of Bengal: Implications for the summer monsoon, *Journal of Geophysical Research: Oceans*, *107*(C6), 5-1-5-14, doi:.Siedler, G., J. Church, and J. Gould (2001), *Ocean Circulation and Climate, Observing and modelling the global ocean*, 715 pp., Academic Press.Soldo, Y., D. Le Vine, and P. de Matthaeis (2019), Detection of Residual "Hot Spots" in RFI-Filtered SMAP Data, *Remote Sens.*, *11(24):2935*, doi:10.3390/rs11242935.Song, Q., and Z. Wang (2017), Sea surface salinity observed from the HY-2A satellite, *2017*, 8, doi:10.18063/som.2017.01.004.Stammer, D., M. S. Martins, J. Köhler, and A. Köhl (2021), How well do we know ocean salinity and its changes?, *Progress in Oceanography*, *190*, 102478, doi:.Supply, A., J. Boutin, G. Reverdin, J.-L. Vergely, and H. Bellenger (2020a), Variability of Satellite Sea Surface Salinity Under Rainfall, in *Satellite Precipitation Measurement: Volume 2*, edited by V. Levizzani, C. Kidd, D. B. Kirschbaum, C. D. Kummerow, K. Nakamura and F. J. Turk, pp. 1155-1176, Springer International Publishing, Cham, doi:10.1007/978-3-030-35798-6_34.Supply, A., J. Boutin, J.-L. Vergely, N. Kolodziejczyk, G. Reverdin, N. Reul, and A. Tarasenko (2020b), New insights into SMOS sea surface salinity retrievals in the Arctic Ocean, *Remote*

Sensing of Environment, *249*, 112027, doi:.Supply, A., J. Boutin, J.-L. Vergely, N. Martin, A. Hasson, G. Reverdin, C. Mallet, and N. Viltard (2018), Precipitation Estimates from SMOS Sea-Surface Salinity, *Quarterly Journal of the Royal Meteorological Society*, *144*(S1), 103-119, doi:.Tang, W., S. Yueh, D. Yang, A. Fore, A. Hayashi, T. Lee, S. Fournier, and B. Holt (2018), The Potential and Challenges of Using Soil Moisture Active Passive (SMAP) Sea Surface Salinity to Monitor Arctic Ocean Freshwater Changes, *Remote Sensing*, *10*(6), 869.Tarasenko, A., A. Supply, N. Kusse-Tiuz, V. Ivanov, M. Makhotin, J. Tournadre, B. Chapron, J. Boutin, N. Kolodziejczyk, and G. Reverdin (2021), Properties of surface water masses in the Laptev and the East Siberian seas in summer 2018 from in situ and satellite data, *Ocean Sci.*, *17*(1), 221-247, doi:10.5194/os-17-221-2021.Tranchant, B., E. Remy, E. Greiner, and O. Legalloudec (2019), Data assimilation of Soil Moisture and Ocean Salinity (SMOS) observations into the Mercator Ocean operational system: focus on the El Niño 2015 event, *Ocean Sci.*, *15*(3), 543-563, doi:10.5194/os-15-543-2019.Vazquez-Cuervo, J., C. Gentemann, W. Tang, D. Carroll, H. Zhang, D. Menemenlis, J. Gomez-Valdes, M. Bouali, and M. Steele (2021), Using Saildrones to Validate Arctic Sea-Surface Salinity from the SMAP Satellite and from Ocean Models, *Remote Sensing*, *13*(5), 831.Vialard, J., and P. Delecluse (1998), An OGCM study for the TOGA decade. Part I: Role of salinity in the physics of the western Pacific fresh pool, *J Phys Oceanogr*, *28*(6), 1071-1088, doi:Doi 10.1175/1520-0485(1998)028<1071:Aosftt>2.0.Co;2.Vinogradova, N., et al. (2019), Satellite Salinity Observing System: Recent Discoveries and the Way Forward, *Frontiers in Marine Science*, *6*(243), doi:10.3389/fmars.2019.00243.Yin, X., J. Boutin, and P. Spurgeon (2013), Biases Between Measured and Simulated SMOS Brightness Temperatures Over Ocean: Influence of Sun, *IEEE Journal of Selected Topics in Applied Earth Observations and Remote Sensing*, *6*(3), 1341-1350.Yu, L., F. M. Bingham, T. Lee, E. P. Dinnat, S. Fournier, O. Melnichenko, W. Tang, and S. H. Yueh (2021), Revisiting the Global Patterns of Seasonal Cycle in Sea Surface Salinity, *Journal of Geophysical Research: Oceans*, *126*(4), e2020JC016789, doi:.Yu, L., S. A. Josey, F. M. Bingham, and T. Lee (2020), Intensification of the global water cycle and evidence from ocean salinity: a synthesis review, *Ann Ny Acad Sci*, *1472*(1), 76-94, doi:10.1111/nyas.14354.Yueh, S. H., R. West, W. J. Wilson, F. K. Li, E. G. Njoku, and Y. Rahmat-Samii (2001), Error sources and feasibility for microwave remote sensing of ocean surface salinity, *IEEE Transactions on Geoscience and Remote Sensing*, *39*(5), 1049-1060.Zhu, J. S., B. H. Huang, R. H. Zhang, Z. Z. Hu, A. Kumar, M. A. Balmaseda, L. Marx, and J. L. Kinter (2014), Salinity anomaly as a trigger for ENSO events, *Scientific Reports*, *4*, doi:ARTN 682110.1038/srep06821.

References from the Supporting Information

https://doi.org/10.12770/12777edd12308-14296-14774-b12776f12773-12775b38301cee12718

www.remss.com/missions/smap

https://doi.org/10.1016/j.rse.2020.112027

CATDS (2017), CATDS-PDC L3OS 2P - Daily valid ocean salinity values product from SMOS satellite, edited, pp. .Dinnat, E. P., D. M. Le Vine, J. Boutin, T. Meissner, and G. Lagerloef (2019), Remote Sensing of Sea Surface Salinity: Comparison of Satellite and In Situ Observations and Impact of Retrieval Parameters, *Remote Sensing*, *11*(7), 750.Klein, L., and C. Swift (1977), An improved model for the dielectric constant of sea water at microwave frequencies, *IEEE Transactions on Antennas and Propagation*, *25*(1), 104-111.Meissner, T., F. J. Wentz, and D. M. Le Vine (2018), The Salinity Retrieval Algorithms for the NASA Aquarius Version 5 and SMAP Version 3 Releases, *Remote Sensing*, *10*(7), 1121.Meissner, T., F. J. Wentz, A. Manaster, and R. Lindsley (2019), Remote Sensing Systems SMAP Ocean Surface Salinities [Level 2C], Version 4.0 validated release edited by S. R. Remote Sensing Systems, CA, USA. Available online at , doi:10.5067/SMP40-2SOCS Supply, A., J. Boutin, J.-L. Vergely, N. Kolodziejczyk, G. Reverdin, N. Reul, and A. Tarasenko (2020), New insights into SMOS sea surface salinity retrievals in the Arctic Ocean, *Remote Sensing of Environment*, *249*, 112027, doi:.Zhou, Y., R. H. Lang, E. P. Dinnat, and D. M. L. Vine (2017), L-Band Model Function of the Dielectric Constant of Seawater, *IEEE Transactions on Geoscience and Remote Sensing*, *55*(12), 6964-6974.